Analyzing the brainstem circuits for respiratory chemosensitivity in freely moving mice

Short title: Chemosensitive brainstem neurons in awake mice

Amol Bhandare[1], Joseph van de Wiel[1], Reno Roberts[1], Ingke Braren[2], Robert Huckstepp[1], Nicholas Dale[1]*.

[1]School of Life Sciences, University of Warwick, Coventry, UK

[2]University Medical Center Eppendorf, Vector Facility, Inst. for Exp. Pharmacology and Toxikology, N30, Room 09, Martinistr. 52, 20246 Hamburg, Germany

*Corresponding Author Email: n.e.dale@warwick.ac.uk

Abstract

Regulation of systemic PCO_2 is a life-preserving homeostatic mechanism. In the medulla oblongata, the retrotrapezoid nucleus (RTN) and rostral medullary Raphe are proposed as CO_2 chemosensory nuclei mediating adaptive respiratory changes. Hypercapnia also induces active expiration, an adaptive change thought to be controlled by the lateral parafacial region (pF_L). Here we use GCaMP6 expression and head-mounted mini-microscopes to image Ca^{2+} activity in these nuclei in awake adult mice during hypercapnia. Activity in the pF_L supports its role as a homogenous neuronal population that drives active expiration. Our data show that chemosensory responses in the RTN and Raphe differ in their temporal characteristics and sensitivity to CO_2, raising the possibility these nuclei act in a coordinated way to generate adaptive ventilatory responses to hypercapnia. Our analysis revises the understanding of chemosensory control in awake adult mouse and paves the way to understanding how breathing is coordinated with complex non-ventilatory behaviours.

Introduction

The precise control of breathing is fundamental to the survival of all terrestrial vertebrates. Breathing fulfils two essential functions: provision of oxygen to support metabolism; and removal of the metabolic by-product, CO_2. Rapid and regulated removal of CO_2 is essential because its over-accumulation in blood will result in death from the consequent drop in pH. Understanding of the complexity of the brain microcircuit regulating CO_2 and pH remains incomplete. Whilst the primacy of the ventral medulla surface (VMS) in central chemoreception was described almost 60 years ago, this region contains multiple chemosensory nuclei that are candidates to mediate adaptive control of breathing (Nattie and Li, 1994; Richerson, 1995). This has led to the idea that central chemosensitivity is mediated by a network of chemosensory nuclei distributed throughout the brainstem and extending as far as the limbic system (Huckstepp and Dale, 2011b). Furthermore, there are multiple phenotypes of neurons within single chemosensory nuclei (Huckstepp et al., 2018; Iceman et al., 2014; Iceman and Harris, 2014; Johansen et al., 2015), and even within previously well-defined subpopulations of neurons (Shi et al., 2017; Stornetta et al., 2009).

Recently, brain imaging techniques have been developed to allow recording of activity of defined cell populations in awake, freely-moving animals even in deep brain structures such as the hypothalamus (Ziv and Ghosh, 2015). These methods require: the expression of genetically encoded Ca^{2+} indicators such as GCaMP6 in the relevant neurons; the implantation of gradient refractive index (GRIN) lenses at the correct stereotaxic position; and a head-mounted mini-epifluorescence microscope to enable image acquisition during the free behaviour of the mouse. We have now adapted these methods to enable recording of defined neuronal populations in the rostral medulla oblongata of mice to analyze the chemosensory control of breathing.

In this paper, we study the activity of neurons in the retrotrapezoid nucleus (RTN) (Mulkey et al., 2004; Nattie and Li, 1994; Ramanantsoa et al., 2011) and the rostral medullary raphe (Bradley et al., 2002; Ray et al., 2011; Richerson, 1995). Evidence strongly favours their involvement in the central chemosensory response, but thorough understanding as to how these nuclei contribute to central chemosensitivity has been hampered by the inability to record the activity of their constituent cells in awake freely behaving adult rodents. Instead, neuronal recordings have been made from young (<14d) or adult rodents under anaesthesia. Both of these methods have significant drawbacks -the chemosensory control of breathing matures postnatally; and anaesthesia is known to depress the activity of respiratory neurons and reconfigure the circuit.

We also assess the contribution of the lateral parafacial region (pF_L) to an often-overlooked aspect of the hypercapnic ventilatory response, active expiration. During resting eupneic breathing, there is little active expiration instead the expiratory step involves elastic rebound of the respiratory

muscles to push air out of the lungs. However, when the intensity of breathing is increased e.g. during exercise or hypercapnia, active expiration (recruitment of abdominal muscles to push air out of the lungs) occurs. Mounting evidence suggests the pF_L may contain the expiratory oscillator and that neurons in this nucleus are recruited to evoke active expiration (Huckstepp et al., 2015; Huckstepp et al., 2016; Pagliardini et al., 2011). Nevertheless, the key step of recording activity of these neurons in awake behaving animals and linking it to active expiration has not been achieved.

Our data show the pF_L did not undergo sustained activation during hypercapnia, but instead contributed to acute transient high amplitude expiratory events. We found that neurons in the RTN and Raphe exhibited a range of responses to hypercapnia. Many RTN neurons exhibited fast adapting responses. This response type was less common in the Raphe, and many Raphe neurons exhibited a slower graded response. Our data are consistent with a tiered chemosensory network, with the RTN and Raphe responsible for detecting different aspects of the hypercapnic stimulus. These novel findings illuminate the fundamental functional components of chemosensory nuclei and show that neuronal responses to hypercapnia are considerably more complex than anticipated.

Results

Optical characteristics of the recording system

The GRIN lens has a diameter of 600 μm with a focal plane ~300 μm below the lens (Jennings et al., 2015; Resendez et al., 2016). However, the focal plane varies depending upon the distance between the camera and GRIN lens, which can be altered via a manual turret adjustment to optimise the focus on fluorescent cells. To document the range of focal plane depth in our system, we imaged fluorescent beads entrapped in agarose under two conditions: the turret at its lowest (i.e. camera is against the end of the GRIN lens, and the focal plane is at its closest to the lens) and its maximum setting (i.e. the camera is as far from the end of the GRIN lens as it can be, and the focal plane is at its deepest relative to the lens) (Figure 1-figure supplement 1). The focal depth (in which the beads were sharply focussed) was 100 μm at any single setting and the full focal plane ranged from 150-450 μm below the end of the lens as the turret moved from its lowest to highest setting. The turret setting is given in all figure legends.

Inclusion/exclusion criteria for cells in the study

Following assessment for inclusion/exclusion criteria, data from 18 mice comprising recordings from 194 cells were included for analysis (Figure 1A). As the mice were unrestrained and able to move freely during the recordings, to visualize physical movements during Ca^{2+} analysis high-definition videos of mice were synchronized to the simultaneous plethysmograph and Inscopix Ca^{2+} imaging recordings in Inscopix Data Processing Software and *Spike2*. Our recordings are

performed at a single wavelength (Figure 1B). Therefore, it was essential to verify that any signals result from changes in Ca^{2+} rather than from movement artefacts.

We examined the origins of the changes in fluorescence in three ways. Firstly, we transduced RTN neurons of three mice with AAV-syn-GFP and performed imaging during a hypercapnic challenge (Figure 1C-D, Figure 1-Video 1). This allowed measurement of comparable levels of fluorescence to GCaMP6 to determine whether movement by itself, in the absence of any Ca^{2+} reporter activity, could generate confounding fluorescent signals. Analysis of changes in fluorescence showed only small amplitude (often negative-going) fluctuations. In no case did we observe large increases in fluorescence of the type we routinely observed when GCaMP6 was expressed (e.g. Figure 1E), suggesting that movement *per se* cannot give fluorescence signals that resemble Ca^{2+} signals.

Secondly, we analyzed the movement of the mouse simultaneously with the Ca^{2+} recordings (Figure 1E) via two methods. The first was to analyze the headmount movements in the video recordings of the mouse in the plethysmography chamber using *AnyMaze* tracking software and convert these movements into a colour coded sonogram. The brighter colours in the sonogram indicate headmount movement. The second method analyzed the large excursions on the whole body plethysmography (WBP) trace. These arise artefactually from movement. Comparison of the sonogram based on the WBP trace (WBP Sonogram) and that based on head movement (Mov Sonogram) showed that the two measures correlated well and that large excursions of the WBP trace often coincided with head movement (compare sonograms in Figure 1E). When we examined the GCaMP6 fluorescence in conjunction with the sonograms of head and body movement, we observed that: i) large movements of the head/body did not evoke noticeable changes in GCaMP6 fluorescence (Figure 1Ea,b); ii) GCaMP6 Ca^{2+} signals characterized by a fast rise and exponential decay occurred in the absence of any movement (Figure 1Ec,f); and iii) similar shaped Ca^{2+} signals occurred during movement (Figure 1Ed,e). Together this suggests that movement of the head or body of the animal does not prevent the recording of genuine changes in GCaMP6 fluorescence related to changes in intracellular Ca^{2+}.

Thirdly, we used the same paradigm of stimulation for all experiments as can be seen from the records in Figure 1-figure supplement 2-4. This enabled averaging of the responses aligned either to the onset of hypercapnia, or features of the WBP trace. This averaging brought out consistent features of the presumed Ca^{2+} signals that were temporally related to either the onset of hypercapnia or alterations of breathing. While for the most part we could not record from the same neurons in different recording sessions from the same mouse, we did observe consistent patterns of neuronal firing between recording sessions (Figure 1-figure supplement 5). As movement that could give rise to artefact would not be expected to be similar from recording session to recording session, or from mouse to mouse, the consistency of the patterns of the signals between mice and

recording sessions strongly suggests a true biological rather than artefactual origin of the recorded signals.

In some cases, it was possible to identify the same neuron from recording sessions on different days in the same mouse. This was only the case in a minority of sessions perhaps because the brainstem is extracranial and more mobile and thus it is harder to reproduce the same exact focal plane between different recording sessions. When we were able to identify the same neurons their activity patterns were remarkably similar between separate recording sessions (Figure 1-figure supplement 6). This gives further confidence that the observed patterns are a reflection of biological properties.

Finally, we made recordings from anaesthetized mice (Figure 1F and Figure 4-figure supplement 1). In this case movement artefacts cannot be a potential confounding factor. To elicit neural activity, we induced electrographic seizures via intraperitoneal kainic acid injection in mice in the absence of any behavioural seizure movements such as partial (including forelimb or hindlimb) or whole body continuous clonic seizures (Figure 1-Video 2). After ~ 70 minutes this resulted in perturbations of the WBP trace and correlated Ca^{2+} activity in the RTN neurons, presumably denoting the invasion of seizures into this nucleus. Detailed examination revealed that the fluorescence changes were of two types: i) transients with a fast rise and exponential fall; and ii) slower sustained changes (Figure 1G). This is an important observation as it shows that we expect to see two types of genuine Ca^{2+} signal in recordings from freely-moving mice: fast transients with an exponential decay phase, that may sum together and slower more gradual rises.

Movements of the visual field, evident during most recordings, were corrected for via the Inscopix motion correction software to allow ROI-based measurement of fluorescence to remain in register with the cells during the recording. Where movement artefacts persisted following motion correction, in some cases it was possible to draw additional ROIs over a high contrast area devoid of fluorescent cells, such as the border of a blood vessel. This allowed for a null signal to be subtracted from the GCaMP signal (Figure 7E) thus providing the neuronal Ca^{2+} transients free of movement artefact. If there was too much uncompensated motion artefact, so that we could not clearly analyze Ca^{2+} signals, we excluded these recordings from quantitative analysis (details given in Figure 1A). GCaMP6 signals were only accepted for categorization if the following criteria were met: 1) the features of the cell (e.g. soma, large processes) could be clearly seen; 2) they occurred in the absence of movement of the mouse or were unaffected by mouse movement; 3) fluorescence changed relative to the background; 4) the focal plane had remained constant as shown by other nonfluorescent landmarks (e.g. blood vessels). Applying these criteria left 144/194 cells eligible for study. All of the recordings that were included are shown in Figure 1-figure supplements 2-4. The activity of the cells fell into the following categories:

Inhibited (I): Displayed spontaneous Ca^{2+} activity at rest, which was greatly reduced during both 3 and 6% inspired CO_2 and could exhibit rebound activity following the end of the hypercapnic episode.

Excited - adapting (E_A): Silent or with low level activity at rest and showed the greatest Ca^{2+} activity in response to a change in 3% inspired CO_2. Following an initial burst of activity, they were either silent or displayed lower level activity throughout the remainder of the hypercapnic episode. These cells often exhibited rebound activity following the end of the hypercapnic episode due to suppression by higher CO_2 levels. These cells essentially encoded the beginning and end of hypercapnia.

Excited - graded (E_G): Silent or with low level activity at rest and displayed an increase in Ca^{2+} activity at 3% inspired CO_2 with a further increase in activity at 6% that returned to baseline upon removal of the stimulus. These cells encoded the level of inspired CO_2.

Tonic (T): Displaying spontaneous Ca^{2+} activity throughout the recording that was unaffected by the hypercapnic episode but could provide tonic drive to the respiratory network.

Sniff-coding (Sn): Displayed elevated Ca^{2+} signals correlated with exploratory sniffing.

Expiratory (Exp): Displayed elevated Ca^{2+} signals correlated with large expiratory events.

Non-coding (NC): Displayed low frequency or sporadic Ca^{2+} activity that was neither tonic in nature nor had any discernable activity that related to the hypercapnic stimulus or any respiratory event.

Non-coding respiratory related (NC-RR): Displayed Ca^{2+} activity that did not code the hypercapnic stimulus, but it was instead related to variability in breathing frequency.

Our categorisation of neurons into these types was supported by a two-component analysis in which we plotted the change in Ca^{2+} activity (from baseline) elicited by 6% inspired CO_2 versus the change in Ca^{2+} activity elicited by 3% inspired CO_2. E_A neurons as they showed more activity at 3% compared to 6% CO_2 should cluster below the line of identity (x=y), whereas E_G neurons as they respond more strongly to 6% than 3% should cluster above the line of identity. *NC* neurons as they did not show a response to hypercapnia should be clustered around the origin (x=y=0), and the *I* neurons should be clustered in the quadrant where the change in Ca^{2+} activity to both stimuli is negative. This analysis shows that the different classes of neurons in both the RTN and Raphe do indeed cluster in the appropriate regions of the graph (Figure 1-figure supplement 7).

Chemosensory responses in the RTN

As the RTN contains chemosensitive glia and neurons (Gourine et al., 2010; Mulkey *et al.*, 2004; Nattie and Li, 1994; Ramanantsoa *et al.*, 2011), and is neuroanatomically diverse (Shi *et al.*, 2017; Stornetta *et al.*, 2009), we began by targeting all neurons of the RTN with a synapsin-GCaMP6s AAV (Figure 2A-C); a necessary step to enable their imaging during free behaviour via a mini-

headmounted microscope (Figure 1B). The localization of successful and accurate transduction was confirmed posthoc by using choline acetyltransferase (ChAT) staining to define the facial nucleus and the location of the transduced cells (Figure 2B), with ~7% (9/132) of transduced neurons in the focal plane of the microscope co-labelled with ChAT (Figure 2C). The lens track terminated under the caudal pole of the facial nucleus, containing the highest number of neurons (Figure 2B), with the focal plane 150-450 μm below that, covering the dorso-ventral extent of the RTN (Figure 1-figure supplement 1). Therefore, our viral transduction and lens placement allowed us to record from the RTN. In some mice (n=3), we further checked the identity of transduced neurons by examining whether they expressed neuromedin B (NMB), a marker specific to Phox2b chemosensory neurons in the RTN (Figure 2D, Figure 2 -figure supplement 2) (Li et al., 2016; Shi *et al.*, 2017). We found 43% (40/93) of NMB+ cells in the RTN were also transduced with GCaMP6, and 20% (40/204) of GCaMP+ neurons in the RTN were NMB+. Thus, we transduced nearly half of the NMB+ neurons, and if the fluorescence imaging sampled transduced cells randomly and without bias to cell type, roughly 1 in 5 of cells recorded would have been of this phenotype.

After assessing the quality of recordings, we retained Ca^{2+} activity traces from 98 RTN neurons in 9 mice (Figure 1A). There was a wide variety of neuronal responses to the hypercapnic challenge (Figure 1-figure supplement 2). While we observed 4/98 neurons exhibited a graded response to hypercapnia (E_G, Figure 2F, G, Figure 2-Video 1), a much greater number (27/98) were of the adapting subtype (E_A, Figure 2H, I, Figure 2-Video 2). This adapting response may also be physiologically meaningful, as it matched the time course of changes in V_E calculated from the WBP records (Figure 2H). In three mice the averaged Ca^{2+} trace of the E_A neurons in each mouse matched the changes in V_T for the same mouse and a plot of V_T versus F/F_0 for the Ca^{2+} signal gave a positive correlation (Figure 2J, and Supplementary file 1). This correspondence between features of the responses in these neurons and the adaptive ventilatory response, supports the hypothesis that these are a physiologically important class of chemosensitive neurons. An alternative explanation that the rates of Ca^{2+} sequestration greatly increased during hypercapnia such that Ca^{2+} levels fell even although firing rates increased can be excluded by examining the dynamics of individual Ca^{2+} transients. The rise time of these transients reflects the rate of Ca^{2+} influx, and the exponentially-falling decay phase the rate of Ca^{2+} extrusion or sequestration. Comparison of these transients before, during and after the hypercapnic stimulus shows that these transients do not change in shape (Figure 2H, Figure 2-figure supplement 2).

A further 5/98 neurons were inhibited during hypercapnia (Figure 3A, C, blue traces and Figure 3-Video 1). These neurons displayed spontaneous Ca^{2+} activity during normocapnia, but were abruptly silenced during hypercapnia (Figure 3C). We recorded from sniff-coding (Sn) neurons, 3/98, which showed elevated Ca^{2+} signals correlated with sniffing (Figure 3A, B). In sniff-coding

neurons, Ca^{2+} activity coincided with perturbations of the plethysmography traces (increase in respiratory frequency, increase of tidal volume, presence of expiration, Figure 3B and Figure 3-Video 1). Analysis of the onset of the Ca^{2+} signal relative to the start of the sniff, showed that, on average, activity in these neurons preceded the sniff by 0.4-0.8 s (Figure 3D). The temporal correlation between the sniff-coding neurons and the sniff was further confirmed by averaging the Ca^{2+} recordings from multiple sniffs (Figure 3E). Interestingly the different functional types of neuron are clustered adjacent to each other (Figure 3F).

Additionally, 5/98 neurons which were tonically active but did not encode any information about hypercapnia (T, Figure 4A, Figure 4-Video 1). Tonically active neurons in the RTN could provide background excitation to the respiratory network. 35/98 neurons showed sporadic activity that did not correlate with CO_2 (NC, Figure 4B) and a further 19/98 neurons that did not encode CO_2 levels but displayed Ca^{2+} signals that were correlated to changes in respiratory frequency and were generally silent when tidal volume was at its greatest (NC-RR, Figure 4C).

In summary for RTN neurons: ~40% (39/98) had activity patterns that were in some way modulated by CO_2. The majority of these neurons, 69% (27/39), displayed an adaptive response to CO_2, thus marking the onset of hypercapnia. Only a minority of neurons, 10% (4/39), encoded the magnitude of hypercapnia and a similar minority (13%; 5/39) were active and inhibited throughout the hypercapnic episode. Interestingly, we found a small number of sniff-activated neurons, which may be from the most rostral and ventral aspect of the retrofacial nucleus, which overlaps with the most caudal and dorsal aspect of the RTN (Deschenes et al., 2016; Kurnikova et al., 2018).

Effect of anaesthesia on RTN chemosensory responses

Until now most investigation of RTN chemosensory responses at adult life stages has been in anaesthetised preparations. We therefore examined the effect of deep anaesthesia on the activity of RTN neurons before and during chemosensory stimuli (Figure 4-figure supplement 1). As might be expected, compared to the awake state, urethane anaesthesia had a deeply suppressive effect on the spontaneous activity of all RTN neurons. Whereas almost all neurons displayed spontaneous activity, there was hardly any activity under anaesthesia (Figure 4-figure supplement 1A-B). Furthermore, the responses to hypercapnia were greatly blunted, with many neurons simply being unresponsive. When we examined those neurons that retained a chemosensory response to hypercapnia in the anesthetised state, these responses differed from those that the same neurons showed in the awake state (Figure 4-figure supplement 1C). For example, cells displaying a graded response to hypercapnia under anaesthesia were classified as non-coding respiratory related (NC-RR) or non-coding (NC) in the awake state.

Chemosensory responses in the medullary raphe

As the medullary Raphe contains multiple neuronal types which display functionally different CO_2 responses *in vitro* (Bradley *et al.*, 2002; Ray *et al.*, 2011; Richerson, 1995) and *in vivo* (Veasey et al., 1995), we next examined whether the activity of neurons in the rostral Raphe magnus and pallidus could be altered by CO_2 (Figure 5). We drove expression of GCaMP6s with a synapsin promoter (n=2 mice; Figure 5A-C). Assessing the ability of this construct to transduce serotonergic neurons in this nucleus, we found that 57/113 (50%) of the transduced neurons in the focal plane of the microscope were TPH+ (tryptophan hydroxylase; a marker of serotonergic neurons) (Figure 5D). As there are also GABAergic neurons (Iceman *et al.*, 2014; Iceman and Harris, 2014), and non-serotonergic NK1R neurons in the Raphe (Hennessy et al., 2017; Iceman and Harris, 2014), we also specifically targeted the serotonergic neurons by driving GCaMP6 expression with a SERT (slc27a4) promoter (n=4 mice, Figure 5E-F). Post-hoc immunocytochemistry showed that all neurons in the optical pathway of the microscope (Figure 5E) which expressed GCaMP6s co-localised with TPH. We recorded 9 synapsin GCaMP6s neurons and 17 SERT GCaMP6s neurons.

As in the RTN, we found there were multiple categories of CO_2-dependent responses (Figure 1-figure supplement 3). A frequently observed class of neurons (8/26) exhibited a graded response to CO_2 (E_G, Figure 5G, H and Figure 5-Video 1, synapsin). 4/26 neurons showed the adapting response (E_A, Figure 5G). The commonest class of neurons in our dataset was inhibited by CO_2 (10/26, all from mice transduced with GCaMP under the SERT promoter, Figure 6A, B, Figure 6-Video 1 SERT). The remaining 4/26 neurons displayed activity that was unaffected by hypercapnia (NC, Figure 6C).

In summary, 85% (22/26) of Raphe neurons had Ca^{2+} activity patterns that were modulated by CO_2. Interestingly, unlike the RTN which showed considerable bias toward the E_A functional type, E_A neurons were much less prevalent in the Raphe (only 15%), with E_G (31%), and I (38%) being the most common types of response we observed. In the Raphe, there were no tonically active neurons or neurons that were co-active with any non-respiratory related orofacial movements such as sniffing.

Expiratory activity of neurons in the pF_L

Neurons of the pF_L, lateral and adjacent to the RTN, have been proposed as the expiratory oscillator (Huckstepp *et al.*, 2015; Huckstepp *et al.*, 2016). Under resting conditions, eupneic breathing, with the exception of during REM sleep (Andrews and Pagliardini, 2015), does not involve active expiration, so the neurons of the pF_L are largely silent. A hypercapnic stimulus causes an increase in respiratory frequency, tidal volume and also the onset of active expiration (Huckstepp *et al.*, 2015). We therefore transduced neurons of the pF_L in 3 mice with the synapsin-GCaMP6f construct (Figure 7A-D) and observed their responses during a hypercapnic stimulus (Figure 7F, Figure 1-figure supplement 4). We found that the Ca^{2+} activity reflected changes in

respiratory frequency and tidal volume with surprising fidelity (compare grey trace (*f*R) with GCaMP traces in Figure 7F). Closer inspection revealed the temporal relationship between Ca^{2+} activity and changes in the plethysmographic traces (Figure 7G). Whilst Ca^{2+} activity in the pF_L neurons on average preceded an increase in tidal volume and respiratory frequency by ~0.4 s, some neurons showed Ca^{2+} activity only after changes in tidal volume and respiratory frequency had occurred (Figure 7H-J). This time separation was independent of the level of inspired CO_2 (Figure 7I, J). These characteristics are more compatible with a correlative rather than a causal relationship between the activation of pF_L neurons and changes in tidal volume and respiratory frequency.

When we specifically studied the incidence of active expiration, we found that Ca^{2+} activity in pF_L neurons always preceded a change in the expiratory activity (Figure 7H-M). Importantly, the time delay between activity in the pF_L neurons and active expiration was sensitive to inspired CO_2 (Figure 7K-M). At 6% inspired CO_2 this time difference was ~0.5 s. (Figure 7K, L), while at 9% inspired CO_2 the time interval shortened to ~0.3 s (Figure 7K, M). In all 20 neurons in the pF_L that exhibited activity, this activity preceded active expiration. This timing is consistent with a causal rather than a correlative link between neuronal activity in the pF_L and induction of active expiration. Post-hoc immunocytochemistry showed that a small population of neurons which expressed GCaMP6 co-localised with ChAT (2/71, 1.5%, Figure 7B, D) and were located in the focal plane of the microscope (Figure 7B). These neurons either displayed expiratory-linked activity or more likely were silent and would have been excluded from our dataset, given no other responses other than expiratory activity were recorded in this region.

Discussion

Limitations

We have recorded the intracellular Ca^{2+} signal from neurons present in the RTN and Raphe. The summation and temporal variation of the signal will depend on the Ca^{2+} buffering/extrusion systems within the cell, the density and activation properties of Ca^{2+} permeable channels, and whether Ca^{2+} may additionally be released from intracellular stores. Therefore, this Ca^{2+} signal cannot tell us the precise firing rates or dynamics of the neuronal activity, and so is an imprecise proxy of neuronal activity. Despite this imperfection, Ca^{2+} activity of neurons is a widely used to assess their electrical activity (Chen et al., 2013; Dana et al., 2019; Huang et al., 2021). We verified that the rates of Ca^{2+} influx and extrusion or sequestration do not change with the hypercapnic stimulus by examining individual Ca^{2+} transients before, during and after hypercapnia to show that their rise times and decay rates remain unaffected (Figure 2-figure supplement 2). This gives further confidence that the pattern of Ca^{2+} activity reflects the pattern of neuronal firing.

We used GCaMP6s for recording from the RTN and Raphe as this is the most sensitive Ca^{2+} sensor and we did not expect to need to resolve rapidly changing Ca^{2+} signals. For the pF_L we used faster responding, but less sensitive, GCaMP6f to attempt to document cycle by cycle changes in fluorescence, but these were not resolved in the current experiments.

We made our recordings at a single wavelength as this was the capability of the minimicroscopes available at the time of the study. Dual channel versions are now available and these would assist with the treatment and exclusion of movement artefacts e.g. through use of ratiometric imaging at two wavelengths. Nevertheless, our extensive controls for movement artefacts, and data analysis, show that we have resolved real Ca^{2+} signals that reflect different patterns of neuronal firing that are reproducible between across the imaged neuronal population in different recording sessions from a single mouse and recordings between multiple mice. These signals are characterised by the well-documented pattern for true Ca^{2+} signals of a fast onset and a slower exponentially-falling offset.

While we can be confident of the location of the GRIN lens and the volume of tissue in which labelled neurons could have contributed to the observed signals from posthoc analysis, it is important to note that we cannot identify the actual neurons that were recorded in each session. Related to this, we were unable, for the most part, to make consecutive recordings from the same neurons from session to session. We used a genetic targeting strategy that would give broad coverage of all neuronal types within the nuclei. This presents an overview of the different activity patterns that occur during responses to hypercapnia, however it does not allow identification of the responses of specific neuronal subtypes. Now that we have a library of all activity patterns in these regions, more precise genetic targeting of neurons is required to relate phenotype to firing pattern. Given that no single unique genetic marker has yet been identified to mark chemosensory neurons, such an approach would have to utilize intersectional genetics to achieve the necessary level of precision.

Our observations document the different types of neuronal responses to hypercapnia in awake mice. However, we cannot be sure whether these responses were a direct consequence of the chemosensory stimulus, i.e. a direct action of CO_2 or pH on the recorded neurons, or an indirect secondary outcome shaped by the synaptic networks present within the medulla. Additionally, recordings from the same neurons in response to repeated periods of hypercapnia would give further assurance that the activity patterns observed are reproducible responses to hypercapnia at a single cell as opposed to population level.

Chemosensory activity in the rostral medulla of adult mice

For many years the RTN was considered to be a homogeneous population of chemosensory neurons (Guyenet et al., 2010; Nattie and Li, 1994). However, recent neuroanatomical (Li *et al.*, 2016; Shi *et al.*, 2017; Stornetta *et al.*, 2009) and pharmacological (Huckstepp *et al.*, 2018; Li *et al.*, 2016) evidence suggests the region may be more heterogenous than first thought and that functional subdivisions of the RTN may exist in adult rodents. In accordance with this, we found 7 functional subpopulations of neurons. There were two classes of neurons that were excited by CO_2 and indicated an aspect of the hypercapnic stimulus (Figure 2): E_A (the start and end of hypercapnia), and E_G (the presence and magnitude of the hypercapnic stimulus). In addition, there were neurons that were inhibited by hypercapnia (I). Inhibition of RTN neuronal firing by hypercapnia has been previously observed (Cleary et al., 2021; Nattie et al., 1993b; Ott et al., 2011).

We found the majority of neurons (from 5 different mice) in our recordings from the RTN were of the E_A subtype i.e. they responded to the initial increase in inspired CO_2 but did not maintain their activation. In some of these neurons there could be a further small increase in activity at the transition of inspired CO_2 from 3 to 6%. This suggests that in these neurons some aspect of the sensory response adapts or fatigues, or they are subject to delayed CO_2-dependent feedback inhibition that depresses their activity. It is notable that in many of these neurons, activity increased following removal of the hypercapnic stimulus. This activation during transitions at the beginning and end of a stimulus is reminiscent of a multitude of rapidly adapting sensory neurons (e.g., rapidly adapting pulmonary receptors (Widdicombe, 1954), Pacinian and Meissner corpuscles (Vallbo and Johansson, 1984)). This could be due to rapid removal of sensory adaptation followed reactivation and rebound activity as the arterial CO_2 levels moves back to resting levels.

While adapting responses to hypercapnia have not been recognised before, the Phox2b+ neurons of the RTN have been subdivided into types 1 and 2 on the basis of their pH sensitivity (Lazarenko et al., 2009). Examination of the response characteristics of the example type 1 neuron illustrated in this paper shows that it displayed an adapting response to acidification, taking 30-40s to decline from peak firing to a steady state baseline (Lazarenko *et al.*, 2009). By contrast the example type 2 neuron shows a sustained graded response (Lazarenko *et al.*, 2009), similar to that reported for a Phox2B+ neuron in an earlier publication (Stornetta et al., 2006). A similar subdivision has been made for acutely isolated Phox2b+ neurons. *In vitro*, type 1 neurons also appear to display an adapting response to acidification suggesting that it may be an intrinsic property (Wang et al., 2013). We tentatively suggest that the adapting neurons (E_A) may therefore correspond to type 1 Phox2b+ neurons, however this would require further direct experimental evidence to substantiate this point.

We found only 4 neurons (from 3 different mice) that exhibited a graded response to CO_2 (E_G). Although these neurons were in the minority, their graded responses to hypercapnia were very similar in time course to those previously described for Phox2b+ RTN neurons in the anaesthetised adult rat (Stornetta *et al.*, 2006) and they might correspond to the type 2 Phox2b+ neurons (Lazarenko *et al.*, 2009). The comparative rarity of the E_G neurons was not due to weak responses to hypercapnia which were very robust in the awake mice (note the raw whole body plethysmography [WBP] traces in Figs 2, 3, 4 and Figure 4-figure supplement 2A). Nor was it due to a technical issue that prevented us from seeing neural activity, as 1) the lens placement was sufficient to image the most superficial aspect of the RTN where the Phox2b neurons lie (Mulkey *et al.*, 2004; Shi *et al.*, 2017; Stornetta *et al.*, 2009), and 2) induction of a seizure in anesthetised mice gave clear Ca^{2+} activity in the RTN neurons when seizures occurred and altered respiratory activity (Figure 1F, G). The possibility that the serotype of the AAV (AAV-9) did not transduce the chemosensory neurons of the RTN seems remote, as others have demonstrated its efficacy for these neurons (Hérent et al., 2021). Although we recorded from 98 RTN neurons in 9 mice, we cannot completely exclude that some unknown aspect of the recording set up may have prevented us from seeing all types of neurons and might have led to comparative under-representation of the E_G subtype in our dataset.

The respiratory network, and with it the hypercapnic ventilatory response, changes with development (Huckstepp and Dale, 2011b). Chemosensory responses become less dependent on Phox2B+ neurons of the RTN by 3 months of age when those neurons are genetically ablated (Ramanantsoa *et al.*, 2011). Acute chemical lesions of the RTN that remove almost all NMB+ neurons, greatly perturbed central chemosensory responses at adult stages, however this was not seen with smaller lesions that preserved a little under half of the NMB+ neurons (Souza et al., 2018). A lesioning strategy, be it chemical or genetic, cannot discriminate between a direct chemosensory function and a relay function of this nucleus. The majority of evidence for the responses of RTN neurons, and in particular the Phox2B+ neurons, to hypercapnic stimuli comes from neonatal or young juvenile animals (Mulkey *et al.*, 2004; Ramanantsoa *et al.*, 2011). Here we are investigating chemosensory mechanism in the adult after the system has fully matured. It is possible that the nature of the chemosensory responses change, and the E_A neuronal phenotype emerges at adult stages. It is notable that even in the cells classified as E_G there is a transient enhancement of activity immediately following the imposition of hypercapnia (Figure 2F, G) suggesting that detection of change in PCO_2 is an important role for RTN neurons.

A second possibility is that much of prior evidence for RTN chemosensory responses depends heavily on recordings from anaesthetized animals and that anaesthesia alters the dynamics of neuronal responses to CO_2. When we compared RTN responses in awake and anaesthetized animals we found that deep urethane anaesthesia dramatically changed neuronal firing patterns

before and during hypercapnia (Figure 4-figure supplement 1). While the choice of anaesthetic agent and depth of anaesthesia is likely to alter the degree to which RTN neurons retain their natural activity, our recordings suggest that studies of chemosensory responses in anaesthetised preparations should be interpreted with caution.

These possibilities are not mutually exclusive and it is likely that they may all contribute to the relatively low proportion of neurons of the E_G subtype in our dataset. Unexpectedly, whilst we recorded from sniff activated neurons, we did not find any neurons with sigh related activity, which may be due to their sparsity in number (Li *et al.*, 2016). Therefore, more recordings may be necessary to uncover further functional subpopulations within the RTN region.

Several lines of evidence have suggested the importance of medullary Raphe serotonergic neurons in mediating respiratory chemosensitivity: the proximity of raphe neuron processes to blood vessels (Bradley *et al.*, 2002); the correspondence of the location of CO_2-dependent ATP release at the medullary surface and the raphe neurons (Bradley *et al.*, 2002; Gourine et al., 2005); suppression of the medullary raphe by isofluorane (Johansen *et al.*, 2015; Ray *et al.*, 2011) which matches the reduction in the overall hypercapnic ventilatory response; and most compellingly the observation that inhibition of their activity via inhibitory DREADD receptors removes ~40% of the total adaptive ventilatory response in awake mice (Ray *et al.*, 2011). There were two classes of neuron excited by CO_2 and these marked the presence and magnitude of the hypercapnic stimulus (E_G) and the start of the hypercapnic episode (E_A), supports the hypothesis that the Raphe acts as a primary chemosensory nucleus.

Of the 2 known serotonergic subtypes in the Raphe, NK1R negative serotonergic neurons project to areas responsible for CO_2 integration (Brust et al., 2014), whereas NK1R positive serotonergic neurons project to motor nuclei responsible for airway patency and co-ordination, and diaphragmatic movements (Hennessy *et al.*, 2017). Interestingly both subtypes project to the preBötC (Brust *et al.*, 2014; Hennessy *et al.*, 2017). Furthermore, both serotonergic and GABAergic raphe neurons project to the pF_L (Silva et al., 2020), with serotonergic neurons also innervating areas that influence expiration, namely the C1 (Malheiros-Lima et al., 2020), and NTS (Silva et al., 2019). Therefore, Raphe neurons are well placed to have far-reaching effects on breathing.

While both the RTN and Raphe have a high proportion of neurons that can be activated by CO_2, there are interesting differences in the nature of the responses that we observed (Figure 8A). The majority of RTN neurons that we observed were of the E_A subtype i.e. they will encode a change in inspired CO_2 rather than the presence of the entire stimulus. Even the E_G neurons responded to a change in inspired CO_2 with a transient change in Ca^{2+} activity in addition to the graded response.

By contrast the situations was reversed in the Raphe: we observed a greater number of Raphe neurons were of the E_G subtype than the E_A subtype. This may suggest a complementarity between the RTN and Raphe, such that the more superficially located RTN rapidly encodes changes in PCO_2, with the deeper sitting Raphe providing a more sustained and graded response to encode the magnitude. It is noteworthy that plethysmographic changes in breathing are well-known to partially adapt to step changes in inspired CO_2 (illustrated in Figure 2H, J, see also (Bravo et al., 2016)) suggesting that the E_A subtype is physiologically important. The rapid response to a sudden change in inspired CO_2 could plausibly be regarded as a trigger to quick behavioural adaptation that could remove the animal from the source of hypercapnia, or trigger a rapid adjustment in breathing that is sufficient to restore normocapnia.

CO_2-inhibited neurons in the RTN and Raphe have been previously described (Iceman *et al.*, 2014; Nattie et al., 1993a). Our recordings give further evidence for these subtypes in both nuclei. In the Raphe, CO_2 inhibited neurons were thought to be exclusively GABAergic. Our finding that serotonergic Raphe neurons can be inhibited by CO_2 is unexpected. The mechanism of CO_2-dependent inhibition is unclear. One possibility is that a CO_2 activated K^+ channel is present in these cells. An inward rectifier K^+ channel that is activated by CO_2 has been described in HeLa cells (Huckstepp and Dale, 2011a), indicating that this mechanism of intrinsic sensitivity is possible. However, a likelier alternative hypothesis is that the inhibitory action of CO_2 on the serotonergic and GABAergic neurons is indirect and depends upon synaptic connectivity -for example via CO_2-dependent activation of local GABAergic interneurons that are present in the medullary Raphe (Figure 8B).

While the emphasis of chemosensory mechanisms has been on the CO_2/pH-dependent activation of excitatory neurons, CO_2/pH-dependent inhibition of neurons could also be a powerful contributor to the hypercapnic ventilatory reflex (Figure 8A). While we have not demonstrated synaptic connections from any of the classes of neurons we describe, if CO_2-inhibited neurons were to tonically excite neurons that normally inhibit the preBötzinger complex, a process of disinhibition during hypercapnia could result in greater excitation of preBötzinger complex neurons (Figure 8A). RTN and Raphe neurons are known to project to the Bötzinger complex (Morinaga et al., 2019; Rosin et al., 2006), which contains inhibitory neurons (Ezure and Manabe, 1988), whilst RTN neurons are also known to project to inhibitory cells of the preBötC (Yang et al., 2019), which regulate the synchronisation of excitatory bursting and the emergence of the inspiratory rhythm (Ashhad and Feldman, 2020). The CO_2-dependent disinhibition of the inhibitory interneurons in the preBötC could contribute to the emergence of more powerful inspiratory bursts and hence an increase in tidal volume (Figure 8A).

Non-chemosensory mechanisms in the RTN

The RTN showed several forms of Ca^{2+} activity that did not respond to hypercapnia. In support of previous findings (Nattie *et al.*, 1993a), we saw a small population of tonically firing neurons that were unaffected by elevating inspired CO_2. These neurons might provide tonic drive to the respiratory network that drives tidal volume, which is known to originate at least in part from the RTN (Huckstepp *et al.*, 2015). However, in 67/98 of the RTN neurons, we observed some tonic activity during room air breathing. Therefore, about 2/3 of the RTN neurons we imaged could plausibly contribute to tonic drive at rest. In addition to providing drive to basal breathing, tonic activity in neurons may also provide a level of baseline excitation that permits for the system to be more easily manipulated, allowing other respiratory features to be expressed. For example there is an absolute requirement for network wide activity to enable expiratory motor output to occur (Huckstepp *et al.*, 2016). Furthermore, it is well documented that as respiratory network excitation decreases during sleep, sensitivity to CO_2 diminishes leading to lower minute ventilation, a higher resting $PaCO_2$ (Douglas et al., 1982a), and reduced hypercapnic ventilatory responses (Douglas et al., 1982b). Thus, tonic activity in the RTN may be vital to allow a greater sensitivity to CO_2 during wakefullness.

We also found non-coding neurons in the RTN. These neurons could be subdivided into those that displayed Ca^{2+} activity not related to the level of CO_2, nor any abstractable feature on the respiratory recording (NC), and those that had Ca^{2+} activity that matched variations in respiratory output (NC-RR). This latter population were largely silent when V_T was at its greatest but displayed activity when the respiratory frequency was high and the faster ventilatory cycle meant that V_T was smaller. The NC-RR neurons might therefore provide excitation to increase respiratory frequency. The NC sub-population could represent a novel neuronal type in the RTN, or could be a known non-CO_2 coding subpopulation that are likely to have other functions such as those that express high levels neuromedin B (Shi *et al.*, 2017).

Sniffing is a mechanism that allows for olfactory sampling of the air to discern location of smell and to test for irritants before air is taken into the lung. Sniffing is obligatory for odour perception (Mainland and Sobel, 2005), and thus activates the piriform cortex (Sobel et al., 1998a). However, sniffing also causes neuronal activity in the absence of odorants (Sobel *et al.*, 1998a). It activates the hippocampus (Vanderwolf, 2001), and the cerebellum (Sobel et al., 1998b), respectively, likely to prime odour-related memory recall, and co-ordination of movement towards or away from specific odours. Whilst the activation of these brain regions during sniffing has been well documented, the pattern generating microcircuit for sniffing has only recently been identified. Sniffing requires the activation of 2 sets of muscles i) the nasal muscles to open the airway and decrease resistance, allowing more rapid movement of air through the nose, and ii) the respiratory (inspiratory and expiratory) muscles, to draw air in and out of the nasal cavity. The RTN is located adjacent to, and innervates, the facial motor nucleus (Deschenes *et al.*, 2016; Kurnikova *et al.*,

2018). These RTN projections to the facial are directly involved in sniffing (Deschenes *et al.*, 2016) and control of nasal direction during the odour response (Kurnikova *et al.*, 2018). In conjunction the RTN provides significant drive to the preBötC (Rosin *et al.*, 2006), and the pF_L (Zoccal et al., 2018), both of which are integral parts of the sniffing microcircuit (Deschenes *et al.*, 2016; Moore et al., 2013). Therefore, it is not surprising that the sniff pathway originates in, or passes through, the RTN.

Active expiration

The pF_L is thought to be a subsidiary conditional oscillator for expiration that is normally suppressed at rest (Huckstepp *et al.*, 2016). That all pF_L neurons showed the same discharge pattern, supports the hypothesis that the pF_L is comprised of a single homogenous group of neurons acting with a single purpose (Huckstepp *et al.*, 2018). Even though the nucleus appears to integrate information from many nuclei -RTN (Zoccal *et al.*, 2018), C1, (Malheiros-Lima *et al.*, 2020), NTS, rostral pedunculopontine tegmental (Silva *et al.*, 2019) and the preBötC (Huckstepp *et al.*, 2016) -the pF_L appears to be a simple on-off switch, rather than forming complex outputs as we describe in the RTN.

Surprisingly, we found that pF_L neurons were only transiently active during large expiratory efforts, (such as sniffing, sighing, or other forms of brief deep breathing), in contrast to the sustained active expiration previously reported (Huckstepp *et al.*, 2015; Leirao et al., 2018). This may be due to our use of brief periods of graded CO_2 in conscious animals, rather than sustained CO_2 (~1 hour) (Leirao *et al.*, 2018) or use of the vagotomised anaesthetised preparation in prior studies (Huckstepp *et al.*, 2015). Importantly, in the un-anaesthetised, vagi intact, *in situ* preparation of young adult rats, pF_L neurons only displayed a small number of action potentials (~10) during the latter portion of expiratory phase 2 (approximately the final 20 % of the expiratory period) (Magalhaes et al., 2021). In our recordings the expiratory period was ~100 ms at the highest level of CO_2, allowing for 20 ms of pF_L neuronal discharge during times of active expiration. Thus Ca^{2+} signals in pF_L neurons were likely too small to elicit a recordable change in GCaMP fluorescence, except when expiratory efforts were notably large in terms of both duration and amplitude. Furthermore, in contrast to our expectation that pF_L neurons would be phasically active between inspiratory bursts, pF_L neurons exhibited elevated intracellular calcium beginning before, and spanning, the expiratory period.

Concluding remarks

Endoscopic imaging of the activity of the brainstem neurons involved in the control of breathing provides a new way to investigate the neural circuitry for the chemosensory control of breathing in awake adult mice, and to understand how breathing is coordinated with complex non-ventilatory

behaviours. Some components, such as expiratory activity of the pF_L or sniff activity in the RTN, are easy to interpret, whilst others are more complicated. The responses to CO_2 were more heterogeneous in both hSyn+ RTN and hSyn+ and serotonergic Raphe neurons than would be expected from the prior literature. Notably, our dataset of RTN chemosensitive neurons contained a preponderance of the E_A subtype. The E_A neuronal responses are potentially well suited to detect small increases of inspired CO_2 outside the normal range that can occur during normal behavioural conditions. In contrast, the Raphe neurons tended to be active during the entire CO_2 stimulus and conceivably these neurons could take over from RTN neurons during more sustained episodes of hypercapnia. These data provide an intriguing possibility that the chemosensory network is arranged in a hierarchy with each layer conveying a unique range of CO_2.

Materials and Methods

Key Resources Table

Reagent type (species) or resource	Designation	Source or reference	Identifiers	Additional information
gene (Mus musculus)	Promoter of mouse *Slc6a4*, Gene Accession: NM_010484	Genecopoiea	MPRM41232-PG02	
strain, strain background (Mus musculus, male)	wild-type	Jackson Laboratories		C57BL/6J background
cell line (Homo sapiens)	293AAV Cell Line	CellBioLabs	AAV-100	HEK293-T
antibody	(Goat polyclonal) anti-cholineacetyl transferase antibody	Millipore	RRID:AB_262156	(1:100 dilution)
antibody	(Rabbit polyclonal) anti-Tryptophan hydroxylase 2 antibody	Millipore Sigma	RRID:AB_10806898	(1:500 dilution)
antibody	(Rabbit polyclonal) anti-NMB (CENTER) antibody	Sigma-Aldrich	RRID:AB_2619620	(1:1000 dilution)

antibody	(donkey polyclonal) anti-rabbit IgG (H+L) Alexa Fluor® 680	Jackson Immunoresea rch	RRID:AB_2340627	(1:250 dilution)
antibody	(donkey polyclonal) anti-rabbit IgG (H+L) Alexa Fluor® 594	Jackson Immunoresea rch	RRID:AB_2340621	(1:250 dilution)
antibody	(donkey polyclonal) anti-goat IgG (H+L) Alexa Fluor® 568	Abcam	RRID:AB_2636995	(1:250 dilution)
antibody	(donkey polyclonal) anti-goat IgG (H+L) Alexa Fluor® 680	Jackson Immunoresea rch	RRID:AB_2340432	(1:250 dilution)
recombinant DNA reagent	AAV-9: pGP-AAV-syn-GCaMP6s-WPRE.4.641	Addgene, Watertown, MA, USA	BS1-NOSAAV9	Dilution 1:10
recombinant DNA reagent	AAV-DJ: pAAV-SERT-GCaMP6s	This paper	Raphe neuronal specific virus with calcium indicator	Dilution 1:10
recombinant DNA reagent	AAV-9: pGP-AAV-syn-GCaMP6f-WPRE.24.693	Addgene, Watertown, MA, USA	BS3-NXFAAV9	Dilution 1:10
recombinant DNA reagent	pAAV.Syn.GCaMP6s.WPRE.SV40	Addgene, Watertown, MA, USA	Plasmid#100843	
recombinant DNA reagent	AAV packaging plasmid pAAV-DJ, AAV-DJ Helper Free Expression System	Cellbiolabs	VPK-410-DJ	
recombinant DNA reagent	AAV packaging plasmid pHelper, AAV-DJ Helper Free Expression System	Cellbiolabs	VPK-410-DJ	
sequence-based reagent	VC327-4 6s HindIII for	This paper	PCR primers	5´-TTGACTGCCTAAGCTTgccaccatgcatcatcatcatcatcatg 300 nM

sequence-based reagent	VC327-4 6s Afe rev	This paper	PCR primers	5'-GATCTCTCGAGCAGCGCTtcacttcgctgtcatcatttgtacaaact 300 nM
peptide, recombinant protein	PrimeSTAR® GXL DNA Polymerase	Takara Bio Europe SAS	R050A	1 U·µg-1
commercial assay, kit	In-Fusion HD Cloning Kit	Takara Bio Europe SAS	639642	
chemical compound, drug	OptiPrep	PROGEN Biotechnik GmbH	1114542	Iodixanol
commercial assay, kit	2 x qPCRBIO SyGreen Mix Hi-ROX	PCRBiosystems	PB20.12	
chemical compound, drug	kainic acid	Fisher Scientific	15467999	8 $mg \cdot kg^{-1}$ IP
chemical compound, drug	atropine	Westward Pharmaceutical Co.	0641-6006-10	120 $\mu g \cdot kg^{-1}$
chemical compound, drug	meloxicam	Norbrook Inc.		2 $mg \cdot kg^{-1}$
chemical compound, drug	buprenorphine	Reckitt Benckiser		100 µg·kg-1
chemical compound, drug	PEI MAX Hydrochloride Transfection Grade Linear 40,000 mwco)	Polysciences Europe GmbH	24765-1	1 µg·µL-1
software, algorithm	Inscopix Data Processing Software (IDPS)	Inscopix	Python Tools 2.2.6 for Visual Studio 2015	Version: 1.6.0.3225
software, algorithm	Spike2	Cambridge Electronic Design	RRID:SCR_000903	Version: 8.23
software, algorithm	Prism 9	GraphPad	RRID:SCR_002798	Version 9.1.0

software, algorithm	ZEN	Carl Zeiss	RRID:SCR_013672	Version 11.0.0.190

Experiments were performed in accordance with the European Commission Directive 2010/63/EU (European Convention for the Protection of Vertebrate Animals used for Experimental and Other Scientific Purposes) and the United Kingdom Home Office (Scientific Procedures) Act (1986) with project approval from the University of Warwick's AWERB.

Cell Lines

To produce AAV particles, we obtained a proprietary cell line, HEK293AAV cells, directly from CellBioLabs for this study. The certification from CellBioLabs stated the cells' identity and that they were free of microbial contamination. These cells were only used to produce the AAV particles and were not used by themselves to generate any of the data in this study.

AAV-DJ: pAAV-SERT-GCaMP6s Vector particle production and purification

The CMV promoter region was excised from pAAV-GFP (Cellbiolabs) by restriction digest with MluI and ClaI, blunting with Klenow Fragment (TheroScientific) and re-ligation with T4 DNA ligase (ThermoScientific) to generate pAAV-GFP without promoter. A SERT promoter clone was purchased from Genecopoiea (Product ID: MPRM41232-PG02, Symbol: Slc6a4, Species: Mouse, Target Gene Accession: NM_010484, Alias: 5-HTT, AI323329, Htt, SertA). The promoter region was cut out with EcoRI and HndIII and introduced by T4 DNA ligation into the previously modified pAAV-GFP to generate pAAV-SERT. Subsequently, a PCR performed using PrimeStar GLX Polymerase (Takara Clontech) with pAAV.Syn.GCaMP6s.WPRE.SV40 (Addgene Plasmid#100843) as a template (forward primer 5´-TTGACTGCCTAAGCTTgccaccatgcatcatcatcatcatcatg and reverse primer 5´-GATCTCTCGAGCAGCGCTtcacttcgctgtcatcatttgtacaaact) to amplify the GCaMP6s fragment. pAAV-SERT was digested with HindIII and AfeI and the PCR product was inserted by InFusion Cloning (Takara Clontech) to generate pAAV-SERT His-GCaMP6s. Accuracy of all cloning steps was verified by PCR, restriction digests and DNA sequencing analysis.

AAV-DJ pseudotyped vectors were generated by co-transfection of HEK293-AAV cells (Cellbiolabs) with the AAV transfer plasmid pAAV-SERT His-GCaMP6s and the AAV packaging plasmid pAAV-DJ and pHelper (both Cellbiolabs). HEK293AAV cells (Cellbiolabs) were cultivated in Dulbecco's modified Eagle's medium (DMEM, High Glucose, Glutamax) supplemented with 10% (v/v) heat-inactivated fetal calf serum, 0.1 mM MEM Non-Essential Amino Acids (NEAA), 100 U/ml penicillin and 100 µg/ml streptomycin. Tissue culture reagents were obtained from Life Technologies. Briefly, $1x10^7$ HEK293-AAV cells were seeded one day before transfection on 15-cm culture dishes and transfected with 7.5 µg pAAV-DJ, 10 µg pHelper and 6.5 µg pAAV plasmid

per plate complexed with Max-polyethylenimine (PEI, Polysciences) at a PEI:DNA ratio (w/w) of 3:1. After 72 h cells were harvested and resuspended in 5 ml lysis buffer (50 mM Tris base, 150 mM NaCl, 5 mM $MgCl_2$, pH 8.5). After three freeze-thaw cycles, benzonase (Merk; final concentration 50 U/ml) was added and the lysates were incubated for 1 h at 37°C. Cell debris was pelleted and vector containing lysates were purified using iodixanol step gradients. Finally, iodixanol was removed by ultrafiltration using Amicon Ultra Cartridges (50 mwco) and three washes with DPBS.

The genomic titers of DNase-resistant recombinant AAV particles were determined after alkaline treatment of virus particles and subsequent neutralization by qPCR using the qPCRBIO SY Green Mix Hi-Rox (Nippon Genetics Europe GmbH) and an ABI PRISM 7900HT cycler (Applied Biosystems). Vectors were quantified using primers specific for the GCaMP6s sequence (5'-CACAGAAGCAGAGCTGCAG and 5'- actggggaggggtcacag). Real-time PCR was performed in a total volume of 10 µl with 0.3 µM for each primer. The corresponding pAAV transfer plasmid was used as a copy number standard. A standard curve for quantification was generated by serial dilutions of the respective plasmid DNA. The cycling conditions were as follows: 50°C for 2 min, 95°C for 10 min, followed by 35 cycles of 95°C for 15 sec and 60°C for 60 sec. Calculations were done using the SDS 2.4 software (Applied Biosystems).

Virus handling

Raphe and RTN neurons - AAV-9: pGP-AAV-syn-GCaMP6s-WPRE.4.641 at a titre of $1x10^{13}$ GC·ml^{-1} (Addgene, Watertown, MA, USA);

Raphe: AAV-DJ: pAAV-SERT-GCaMP6s at a titre of $1.8x10^{13}$GC·ml^{-1} (University hospital Hamburg-Eppendorf, Hamburg, Germany).

pF_L - AAV-9: pGP-AAV-syn-GCaMP6f-WPRE.24.693 at a titre of $1x10^{13}$ GC·ml^{-1} (Addgene, Watertown, MA, USA).

Viruses were aliquoted and stored at -80°C. On the day of injection, viruses were removed and held at 4°C, loaded into graduated glass pipettes (Drummond Scientific Company, Broomall, PA, USA), and placed into an electrode holder for pressure injection. The AAV-syn-GCaMP6s and AAV-syn-GCaMP6f vectors use the synapsin promoter, and therefore transduced neurons showing higher tropism for the AAV 2/9 subtype, and to a much lesser extent neurons that show low tropism for AAV 2/9 within the injection site, e.g. facial motoneurons, they do not transduce non-neuronal cells. Vector AAV SERT-GCaMP6s was specific for serotonergic neurons.

Viral transfection of RTN, Raphe and pF_L neurons

Adult male C57BL/6 mice (20-30 g) were anesthetized with isofluorane (4%; Piramal Healthcare Ltd, Mumbai, India) in pure oxygen (4 L·min^{-1}). Adequate anaesthesia was maintained with 0.5-2% Isofluorane in pure oxygen (1 L·min^{-1}) throughout the surgery. Mice received a presurgical subcutaneous injection of atropine (120 µg·kg^{-1}; Westward Pharmaceutical Co., Eatontown, NJ,

USA) and meloxicam (2 mg·kg^{-1}; Norbrook Inc., Lenexa, KS, USA). Mice were placed in a prone position into a digital stereotaxic apparatus (Kopf Instruments, Tujunga, CA, USA) on a heating pad (TCAT 2-LV: Physitemp, Clifton, NJ, USA) and body temperature was maintained at a minimum of 33°C via a thermocouple. The head was levelled at bregma, and 2 mm caudal to bregma, and graduated glass pipettes containing the virus were placed stereotaxically into either the RTN, rostral medullary raphe or pF_L (Figure 2A, 5A, and 7A). The RTN was defined as the area ventral to the caudal half of the facial nucleus, bound medially and laterally by the edges of the facial nucleus (coordinates with a 9º injection arm angle: -1.0 mm lateral and -5.6 mm caudal from Bregma, and -5.5 mm ventral from the surface of the cerebellum; Figure 2A). The Raphe was defined as the medial, TPH containing regions level with the caudal face of the facial nucleus: the Raphe Magnus (RMg) was directly above the pyramidal tracts (Py), and the Raphe Pallidus (RPa) was bound laterally by the Py (coordinates with a 9º injection arm angle: 0 mm lateral and -5.8 mm caudal from Bregma, and -5.2 mm ventral from the surface of the cerebellum; Figure 5A). The pF_L was defined as the neurons bound laterally by the spinothalmic tract and medially by the lateral edge of the facial motor nucleus (coordinates with a 9º injection arm angle: -1.8 mm lateral and -5.55 mm caudal from Bregma, and -4.7 mm ventral from the surface of the cerebellum; Figure 7A). The virus solution was pressure injected (<300 nL) unilaterally. Pipettes were left in place for 3-5 minutes to prevent back flow of the virus solution up the pipette track. Postoperatively, mice received intraperitoneal (IP) injections of buprenorphine (100 µg·kg^{-1}; Reckitt Benckiser, Slough, UK). Mice were allowed 2 weeks for recovery and viral expression, with food and water *ad libitum*.

GRIN lens implantation

Mice expressing GCaMP6 were anesthetized with isofluorane, given pre-surgical drugs, placed into a stereotax, and the head was levelled as described above. To widen the lens path whilst producing the least amount of deformation of tissue, a graduated approach was taken; firstly a glass pipette was inserted down the GRIN lens path to a depth 200 µm above where the lens would terminated and left in place for 3 mins; this procedure was then repeated with a blunted hypodermic needle. The GRIN lens (600 µm diameter, 7.3 mm length; Inscopix, Palo Alto, CA, USA) was then slowly inserted at a rate of 100µm·min^{-1} to a depth ~1300 µm above the target site, then lowered at a rate of 50µm·min^{-1} to a depth ~300 µm above the RTN, Raphe or pF_L (coordinates with a 9º injection arm angle: RTN – 1.1 mm lateral and -5.75 mm caudal from Bregma, and -5.3 mm ventral from the surface of the cerebellum; Raphe – 0 mm lateral and -5.95 mm caudal from Bregma, and -5.1 mm ventral from the surface of the cerebellum; pF_L – 1.7 mm lateral and -5.7 mm caudal from Bregma, and -4.6 mm ventral from the surface of the cerebellum). The lens was then secured in place with SuperBond™ (Prestige Dental, Bradford, UK). Postoperatively, mice received buprenorphine, and were allowed 2 weeks for recovery, with food and water *ad libitum*.

Baseplate installation

Mice expressing GCaMP6 and implanted with GRIN lens were anesthetized with isofluorane, given pre-surgical drugs, and placed into a stereotax as described above. To hold the miniaturized microscope during recordings, a baseplate was positioned over the lens and adjusted until the cells under the GRIN lens were in focus. The baseplate was then secured with superbond™, and coated in black dental cement (Vertex Dental, Soesterberg, the Netherlands) to stop interference of the recording from ambient light. Mice were allowed 1 week for recovery, with food and water *ad libitum*.

Ca^{2+} imaging in freely moving mice

All mice were trained with dummy camera and habituated to plethysmography chamber at least twice before imaging. The miniature microscope with integrated 475 nm LED (Inscopix, Palo Alto, CA, USA) was secured to the baseplate. GCaMP6 fluorescence was visualised through the GRIN lens, using nVista 2 HD acquisition software (Inscopix, Palo Alto, CA, USA). Calcium fluorescence was optimised for each experiment so that the histogram range was ~150-600, with average recording parameters set at 10-20 frames/sec with the LED power set to 10-20 mW of light and a digital gain of 1.0-4.0. A TTL pulse was used to synchronize the calcium signalling to the plethysmography trace. All images were processed using Inscopix data processing software (Inscopix, Palo Alto, CA, USA). GCaMP6 movies were ran through: preprocessing algorithm (with temporal downsampling), crop, spatial filter algorithm (0.005 - 0.5 Hz), motion correction and cell identification through manual regions of interest (ROIs) operation to generate the identified cell sets. Cell sets were imported into *Spike2* software for processing.

Plethysmography

Mice were placed into a custom-made 0.5 L plethysmography chamber, with an airflow rate of 1 $l \cdot min^{-1}$. The plethysmography chamber was heated to 31^0C (thermoneutral for C57/BL6 mice). CO_2 concentrations were sampled via a Hitech Intruments (Luton, UK) GIR250 Dual Sensor Gas analyzer or ML206 gas analyzer (ADinstruments, Sydney, Australia) connected to the inflow immediately before entering the chamber. The analyser had a delay of ~15-20 sec to read-out the digital output of gas mixture. Pressure transducer signals and CO_2 measurements were amplified and filtered using the NeuroLog system (Digitimer, Welwyn Garden City, UK) connected to a 1401 interface and acquired on a computer using *Spike2* software (Cambridge Electronic Design, Cambridge, UK). Video data was recorded with *Spike2* software and was synchronised with the breathing trace. Airflow measurements were used to calculate: tidal volume (V_T: signal trough at the end of expiration subtracted from the peak signal during inspiration, converted to mL following calibration and normalized to body weight), and respiratory frequency (*f*R: breaths per minute). Minute ventilation (V_E) was calculated as V_T x *f*R.

Hypercapnia in freely behaving mice

Instrumented mice were allowed ~30 mins to acclimate to the plethysmograph. The LED was activated through a TTL pulse synchronised with the *Spike2* recording and 1 or 3 min of baseline recordings were taken (gas mixture: 0% CO_2 21% O_2 79% N_2). The mice were then exposed to 3 min epochs of hypercapnic gas mixture at different concentrations of CO_2: RTN and Raphe transduced mice were exposed to 3% followed by 6% CO_2, and pF_L transduced mice were exposed to 6% followed by 9% CO_2. All gas mixtures contained 21% O_2 balanced N_2. Following exposure to the hypercapnic gas mixtures, CO_2 levels were reduced back to 0% and calcium signals were recorded for a further 3-4 minutes recovery period.

Hypercapnia and seizure induction in urethane anaesthetised mice

Instrumented mice were anaesthetised with an IP injection of 1.2-1.5 g·kg^{-}1 urethane (Sigma-Aldrich, St Louis, MO, USA) and placed into the plethysmograph. For recording responses of RTN neurons to hypercapnia, the LED was activated and 1 or 3 minute of baseline recording was taken. The mice were then exposed to 2 or 3-minute epochs of hypercapnic gas mixture 3%, 6% and 9% CO_2 (in 21% O_2 balanced N_2) sequentially, as experiments into the chemosensitivity of RTN neurons in mice often use 6% CO_2 in freely behaving experiments but 9% CO_2 in anaesthetised animals. Following exposure to the hypercapnic gas mixtures, CO_2 levels were reduced back to 0% and calcium signals were recorded for a further 3-minute recovery period.

For neurons recorded in the RTN, after completion of hypercapnic responses and a period of rest, baseline Ca^{2+} activity was recorded for 5 minutes. The mice were then injected with a dose of kainic acid (8 mg·kg^{-1} IP) sufficient to induce an electrographic seizures in the absence of any movement from behavioural seizures. Following injection of kainic acid, calcium activity was recorded every alternate 5 minutes to avoid the fluorophore bleaching and concurrently record the calcium activity for a long enough to evidence the effect of induction of seizure on the activity of RTN neurons (at least for 90 min post kainic acid injection).

Preparation of fixed brain slices

Mice were humanely killed by pentobarbital overdose (>100 mg·kg^{-1}) and transcardially perfused with paraformaldehyde solution (4% PFA; Sigma-Aldrich, St Louis, MO, USA). The head was removed and postfixed in PFA (4°C) for 3 days to preserve the lens tract. The brains were removed and postfixed in PFA (4°C) overnight. Brainstems were serially sectioned at 50-70 µm.

Immunohistochemistry

Free-floating sections were incubated for 1 hour in a blocking solution (PBS containing 0.1% Triton X-100 and 5% BSA). The tissue was then incubated overnight at room temperature in

primary antibodies: goat anti-choline acetyl transferase [ChAT; 1:100; Millipore, Burlington, MA, USA] alone for co-labelling with GCaMP6, or rabbit anti-tryptophan hydroxylase [TPH; 1:500; Sigma-Aldrich, St Louis, MO, USA] alone for co-labelling with GCaMP6.

Slices were washed in PBS (6 × 5 mins) and then incubated in a blocking solution to which secondary antibodies were added; donkey anti-rabbit Alexa Fluor 594 (1:250; Jackson Laboratory, Bar Harbor, ME, USA) for co-labelling with GCaMP6, or donkey anti-goat Alexa Fluor 594 (1:250; Jackson Laboratory, Bar Harbor, ME, USA; RTN) for co-labelling with GCaMP6 in RTN tissue or donkey anti-goat Alexa Fluor 568 (1:250; Jackson Laboratory, Bar Harbor, ME, USA) for co-labelling with GCaMP6 in pF_L tissue. The tissue was then incubated 2-4 hours at room temperature. Tissue was washed in PBS (6 × 5 min). Slices were mounted on polysine adhesion slides and were coverslipped with Vectashield Antifade Mounting Medium with DAPI (Vectorlabs, Burlingame, CA, United States).

Heat-induced epitope retrieval and immunohistochemistry for NMB

Slices were mounted onto poly-lysine coated microscope slides and allowed to dry and adhere. Mounted brain sections were added to the pre-heated sodium citrate antigen retrieval buffer (10 mM sodium citrate, 0.05% Tween 20, pH 9.0) and incubated for 15 mins. The mounted brain sections were then removed and washed in PBS.

The tissue was then incubated for 1 hour in a blocking solution. Without washing, the tissue was then incubated overnight at room temperature in blocking solution containing primary antibodies: (goat anti-ChAT [same as above] alone for co-labelling with GCaMP6, or in conjunction with rabbit anti-Neuromedin-B [NMB; 1:100; SAB1301059; Sigma-Aldrich, St Louis, MO, USA] antibody) for co-labelling of ChAT and NMB.

The tissue was then washed in PBS (6 × 5 mins) and incubated for 1 hour in a blocking solution. Without washing, the tissue was then incubated 2 hours at room temperature in blocking solution containing secondary antibodies: donkey anti-rabbit Alexa Fluor 568 (1:250; Invitrogen, Waltham, MA, United States) for co-labelling with GCaMP6, or donkey anti-rabbit Alexa Fluor 488 (1:250; Invitrogen, Waltham, MA, United States) and donkey anti-goat Alexa Fluor 594 (1:250; Invitrogen, Waltham, MA, United States) for co-labelling of ChAT and NMB. Tissue was washed in PBS (6 × 5 min).

Slides were examined using a Zeiss 880 confocal microscope with ZEN acquisition software (Zeiss, Oberkochen, Germany).

Antibody specificity

The antibodies that we used have been independently validated by others in the field: anti-ChAT (Dempsey et al., 2015; Saunders et al., 2015; Zhang et al., 2020); anti-TPH (Pitzer et al., 2015; Quina et al., 2020; Zhong et al., 2017)1; and anti-NMB (Li *et al.*, 2016). The staining patterns we report are highly consistent with these prior studies indicating that these antibodies are specifically recognising their targets with the tissue we have examined. Additionally, we compared NMB immunostaining with *in situ* hybridization patterns for NMB documented in the Allen Brain Atlas and found it to be very similar (Fig 2, Figure Supplement 1).

Acknowledgements

Funding: This work was supported by an MRC Discovery Award MC_PC_15070. ND is a Royal Society Wolfson Research Merit Award Holder. We thank Tamara Sotelo-Hitschfeld for help in the early stages of developing the method.

Competing interests: The authors declare that they have no competing interests.

Data and Materials availability: All data is included in the figures and supplements of this paper.

References

Andrews, C.G., and Pagliardini, S. (2015). Expiratory activation of abdominal muscle is associated with improved respiratory stability and an increase in minute ventilation in REM epochs of adult rats. Journal of Applied Physiology *119*, 968-974. 10.1152/japplphysiol.00420.2015.

Ashhad, S., and Feldman, J.L. (2020). Emergent Elements of Inspiratory Rhythmogenesis: Network Synchronization and Synchrony Propagation. Neuron *106*, 482-497. 10.1016/j.neuron.2020.02.005.

Bradley, S.R., Pieribone, V.A., Wang, W., Severson, C.A., Jacobs, R.A., and Richerson, G.B. (2002). Chemosensitive serotonergic neurons are closely associated with large medullary arteries. Nat Neurosci *5*, 401-402.

Bravo, K., Eugenin, J.L., and Llona, I. (2016). Perinatal Fluoxetine Exposure Impairs the CO2 Chemoreflex. Implications for Sudden Infant Death Syndrome. Am J Respir Cell Mol Biol *55*, 368-376. 10.1165/rcmb.2015-0384OC.

Brust, R.D., Corcoran, A.E., Richerson, G.B., Nattie, E., and Dymecki, S.M. (2014). Functional and developmental identification of a molecular subtype of brain serotonergic neuron specialized to regulate breathing dynamics. Cell Rep *9*, 2152-2165. 10.1016/j.celrep.2014.11.027.

907 Chen, T.W., Wardill, T.J., Sun, Y., Pulver, S.R., Renninger, S.L., Baohan, A., Schreiter, E.R., Kerr,
908 R.A., Orger, M.B., Jayaraman, V., et al. (2013). Ultrasensitive fluorescent proteins for imaging
909 neuronal activity. Nature *499*, 295-300. 10.1038/nature12354.

910 Cleary, C.M., Milla, B.M., Kuo, F.S., James, S., Flynn, W.F., Robson, P., and Mulkey, D.K. (2021).
911 Somatostatin-expressing parafacial neurons are CO(2)/H(+) sensitive and regulate baseline
912 breathing. eLife *10*. 10.7554/eLife.60317.

913 Dana, H., Sun, Y., Mohar, B., Hulse, B.K., Kerlin, A.M., Hasseman, J.P., Tsegaye, G., Tsang, A.,
914 Wong, A., Patel, R., et al. (2019). High-performance calcium sensors for imaging activity in
915 neuronal populations and microcompartments. Nat Methods *16*, 649-657. 10.1038/s41592-019-
916 0435-6.

917 Dempsey, B., Turner, A.J., Le, S., Sun, Q.J., Bou Farah, L., Allen, A.M., Goodchild, A.K., and
918 McMullan, S. (2015). Recording, labeling, and transfection of single neurons in deep brain
919 structures. Physiol Rep *3*. 10.14814/phy2.12246.

920 Deschenes, M., Kurnikova, A., Elbaz, M., and Kleinfeld, D. (2016). Circuits in the Ventral Medulla
921 That Phase-Lock Motoneurons for Coordinated Sniffing and Whisking. Neural Plast *2016*,
922 7493048. 10.1155/2016/7493048.

923 Douglas, N.J., White, D.P., Pickett, C.K., Weil, J.V., and Zwillich, C.W. (1982a). Respiration during
924 sleep in normal man. Thorax *37*, 840-844. 10.1136/thx.37.11.840.

925 Douglas, N.J., White, D.P., Weil, J.V., Pickett, C.K., and Zwillich, C.W. (1982b). Hypercapnic
926 Ventilatory Response in Sleeping Adults. American Review of Respiratory Disease *126*, 758-762.
927 10.1164/arrd.1982.126.5.758.

928 Ezure, K., and Manabe, M. (1988). Decrementing expiratory neurons of the Botzinger complex. II.
929 Direct inhibitory synaptic linkage with ventral respiratory group neurons. Exp Brain Res *72*, 159-
930 166.

931 Gourine, A.V., Kasymov, V., Marina, N., Tang, F., Figueiredo, M.F., Lane, S., Teschemacher, A.G.,
932 Spyer, K.M., Deisseroth, K., and Kasparov, S. (2010). Astrocytes control breathing through pH-
933 dependent release of ATP. Science *329*, 571-575. science.1190721 [pii]
934 10.1126/science.1190721.

935 Gourine, A.V., Llaudet, E., Dale, N., and Spyer, K.M. (2005). ATP is a mediator of chemosensory
936 transduction in the central nervous system. Nature *436*, 108-111. nature03690 [pii]
937 10.1038/nature03690.

938 Guyenet, P.G., Stornetta, R.L., and Bayliss, D.A. (2010). Central respiratory chemoreception. The
939 Journal of comparative neurology *518*, 3883-3906. 10.1002/cne.22435.

940 Hennessy, M.L., Corcoran, A.E., Brust, R.D., Chang, Y., Nattie, E.E., and Dymecki, S.M. (2017).
941 Activity of Tachykinin1-Expressing Pet1 Raphe Neurons Modulates the Respiratory Chemoreflex.
942 The Journal of Neuroscience *37*, 1807. 10.1523/JNEUROSCI.2316-16.2016.

943 Hérent, C., Diem, S., Fortin, G., and Bouvier, J. (2021). Upregulation of breathing rate during
944 running exercise by central locomotor circuits. bioRxiv, 2021.2007.2028.453983.
945 10.1101/2021.07.28.453983.

946 Huang, L., Ledochowitsch, P., Knoblich, U., Lecoq, J., Murphy, G.J., Reid, R.C., de Vries, S.E.,
947 Koch, C., Zeng, H., Buice, M.A., et al. (2021). Relationship between simultaneously recorded
948 spiking activity and fluorescence signal in GCaMP6 transgenic mice. eLife *10*.
949 10.7554/eLife.51675.

950 Huckstepp, R.T., Cardoza, K.P., Henderson, L.E., and Feldman, J.L. (2015). Role of parafacial
951 nuclei in control of breathing in adult rats. J Neurosci *35*, 1052-1067. 10.1523/jneurosci.2953-
952 14.2015.

953 Huckstepp, R.T., and Dale, N. (2011a). CO2-dependent opening of an inwardly rectifying K+
954 channel. Pflugers Arch *461*, 337-344. 10.1007/s00424-010-0916-z.

955 Huckstepp, R.T., and Dale, N. (2011b). Redefining the components of central CO2
956 chemosensitivity--towards a better understanding of mechanism. J Physiol *589*, 5561-5579.
957 10.1113/jphysiol.2011.214759.

958 Huckstepp, R.T., Henderson, L.E., Cardoza, K.P., and Feldman, J.L. (2016). Interactions between
959 respiratory oscillators in adult rats. eLife *5*. 10.7554/eLife.14203.

960 Huckstepp, R.T.R., Cardoza, K.P., Henderson, L.E., and Feldman, J.L. (2018). Distinct parafacial
961 regions in control of breathing in adult rats. PloS one *13*, e0201485.
962 10.1371/journal.pone.0201485.

963 Iceman, K.E., Corcoran, A.E., Taylor, B.E., and Harris, M.B. (2014). CO2-inhibited neurons in the
964 medullary raphe are GABAergic. Respir Physiol Neurobiol *203*, 28-34. 10.1016/j.resp.2014.07.016.

965 Iceman, K.E., and Harris, M.B. (2014). A group of non-serotonergic cells is CO2-stimulated in the
966 medullary raphe. Neuroscience *259*, 203-213. 10.1016/j.neuroscience.2013.11.060.

967 Jennings, J.H., Ung, R.L., Resendez, S.L., Stamatakis, A.M., Taylor, J.G., Huang, J., Veleta, K.,
968 Kantak, P.A., Aita, M., Shilling-Scrivo, K., et al. (2015). Visualizing hypothalamic network dynamics
969 for appetitive and consummatory behaviors. Cell *160*, 516-527. 10.1016/j.cell.2014.12.026.

970 Johansen, S.L., Iceman, K.E., Iceman, C.R., Taylor, B.E., and Harris, M.B. (2015). Isoflurane
971 causes concentration-dependent inhibition of medullary raphe; 5-HT neurons in situ. Autonomic
972 Neuroscience: Basic and Clinical *193*, 51-56. 10.1016/j.autneu.2015.07.002.

973 Kurnikova, A., Deschênes, M., and Kleinfeld, D. (2018). Functional brain stem circuits for control of
974 nose motion. Journal of neurophysiology *121*, 205-217. 10.1152/jn.00608.2018.

975 Lazarenko, R.M., Milner, T.A., Depuy, S.D., Stornetta, R.L., West, G.H., Kievits, J.A., Bayliss, D.A.,
976 and Guyenet, P.G. (2009). Acid sensitivity and ultrastructure of the retrotrapezoid nucleus in
977 Phox2b-EGFP transgenic mice. J Comp Neurol *517*, 69-86. 10.1002/cne.22136.

978 Leirao, I.P., Silva, C.A., Jr., Gargaglioni, L.H., and da Silva, G.S.F. (2018). Hypercapnia-induced
979 active expiration increases in sleep and enhances ventilation in unanaesthetized rats. J Physiol
980 *596*, 3271-3283. 10.1113/JP274726.

981 Li, P., Janczewski, W.A., Yackle, K., Kam, K., Pagliardini, S., Krasnow, M.A., and Feldman, J.L.
982 (2016). The peptidergic control circuit for sighing. Nature *530*, 293-297. 10.1038/nature16964.

983 Magalhaes, K.S., da Silva, M.P., Mecawi, A.S., Paton, J.F.R., Machado, B.H., and Moraes, D.J.A.
984 (2021). Intrinsic and synaptic mechanisms controlling the expiratory activity of excitatory lateral
985 parafacial neurones of rats. J Physiol *599*, 4925-4948. 10.1113/JP281545.

986 Mainland, J., and Sobel, N. (2005). The Sniff Is Part of the Olfactory Percept. Chemical senses *31*,
987 181-196. 10.1093/chemse/bjj012.

988 Malheiros-Lima, M.R., Silva, J.N., Souza, F.C., Takakura, A.C., and Moreira, T.S. (2020). C1
989 neurons are part of the circuitry that recruits active expiration in response to the activation of
990 peripheral chemoreceptors. eLife *9*. 10.7554/eLife.52572.

991 Moore, J.D., Deschênes, M., Furuta, T., Huber, D., Smear, M.C., Demers, M., and Kleinfeld, D.
992 (2013). Hierarchy of orofacial rhythms revealed through whisking and breathing. Nature *497*, 205-
993 210. 10.1038/nature12076.

994 Morinaga, R., Nakamuta, N., and Yamamoto, Y. (2019). Serotonergic projections to the ventral
995 respiratory column from raphe nuclei in rats. Neurosci. Res. *143*, 20-30.
996 https://doi.org/10.1016/j.neures.2018.05.004.

997 Mulkey, D.K., Stornetta, R.L., Weston, M.C., Simmons, J.R., Parker, A., Bayliss, D.A., and
998 Guyenet, P.G. (2004). Respiratory control by ventral surface chemoreceptor neurons in rats. Nat
999 Neurosci *7*, 1360-1369.

1000 Nattie, E.E., Fung, M.-L., Li, A., and St. John, W.M. (1993a). Responses of respiratory modulated
1001 and tonic units in the retrotrapezoid nucleus to CO2. Respiration Physiology *94*, 35-50.
1002 https://doi.org/10.1016/0034-5687(93)90055-F.

1003 Nattie, E.E., Fung, M.L., Li, A., and St John, W.M. (1993b). Responses of respiratory modulated
1004 and tonic units in the retrotrapezoid nucleus to CO2. Respir Physiol *94*, 35-50.

1005 Nattie, E.E., and Li, A. (1994). Retrotrapezoid nucleus lesions decrease phrenic activity and CO2
1006 sensitivity in rats. Respir Physiol *97*, 63-77.

1007 Ott, M.M., Nuding, S.C., Segers, L.S., Lindsey, B.G., and Morris, K.F. (2011). Ventrolateral
1008 medullary functional connectivity and the respiratory and central chemoreceptor-evoked
1009 modulation of retrotrapezoid-parafacial neurons. J Neurophysiol *105*, 2960-2975.
1010 10.1152/jn.00262.2010.

1011 Pagliardini, S., Janczewski, W.A., Tan, W., Dickson, C.T., Deisseroth, K., and Feldman, J.L.
1012 (2011). Active expiration induced by excitation of ventral medulla in adult anesthetized rats. J
1013 Neurosci *31*, 2895-2905. 10.1523/jneurosci.5338-10.2011.

1014 Pitzer, M., Lueras, J., Warden, A., Weber, S., and McBride, J. (2015). Viral vector mediated
1015 expression of mutant huntingtin in the dorsal raphe produces disease-related neuropathology but
1016 not depressive-like behaviors in wildtype mice. Brain Res *1608*, 177-190.
1017 10.1016/j.brainres.2015.02.027.

1018 Quina, L.A., Walker, A., Morton, G., Han, V., and Turner, E.E. (2020). GAD2 Expression Defines a
1019 Class of Excitatory Lateral Habenula Neurons in Mice that Project to the Raphe and Pontine
1020 Tegmentum. eNeuro *7*. 10.1523/eneuro.0527-19.2020.

1021 Ramanantsoa, N., Hirsch, M.-R., Thoby-Brisson, M., Dubreuil, V., Bouvier, J., Ruffault, P.-L.,
1022 Matrot, B., Fortin, G., Brunet, J.-F., Gallego, J., and Goridis, C. (2011). Breathing without CO2
1023 Chemosensitivity in Conditional Phox2b Mutants. The Journal of Neuroscience *31*, 12880-12888.
1024 10.1523/jneurosci.1721-11.2011.

1025 Ray, R.S., Corcoran, A.E., Brust, R.D., Kim, J.C., Richerson, G.B., Nattie, E., and Dymecki, S.M.
1026 (2011). Impaired respiratory and body temperature control upon acute serotonergic neuron
1027 inhibition. Science *333*, 637-642. 10.1126/science.1205295.

1028 Resendez, S.L., Jennings, J.H., Ung, R.L., Namboodiri, V.M., Zhou, Z.C., Otis, J.M., Nomura, H.,
1029 McHenry, J.A., Kosyk, O., and Stuber, G.D. (2016). Visualization of cortical, subcortical and deep
1030 brain neural circuit dynamics during naturalistic mammalian behavior with head-mounted
1031 microscopes and chronically implanted lenses. Nat Protoc *11*, 566-597. 10.1038/nprot.2016.021.

1032 Richerson, G.B. (1995). Response to CO2 of neurons in the rostral ventral medulla in vitro. J.
1033 Neurophysiol. *73*, 933-944. 10.1152/jn.1995.73.3.933.

1034 Rosin, D.L., Chang, D.A., and Guyenet, P.G. (2006). Afferent and efferent connections of the rat
1035 retrotrapezoid nucleus. J Comp Neurol *499*, 64-89.

1036 Saunders, A., Granger, A.J., and Sabatini, B.L. (2015). Corelease of acetylcholine and GABA from
1037 cholinergic forebrain neurons. eLife *4*. 10.7554/eLife.06412.

1038 Shi, Y., Stornetta, R.L., Stornetta, D.S., Onengut-Gumuscu, S., Farber, E.A., Turner, S.D.,
1039 Guyenet, P.G., and Bayliss, D.A. (2017). Neuromedin B Expression Defines the Mouse
1040 Retrotrapezoid Nucleus. The Journal of Neuroscience *37*, 11744. 10.1523/JNEUROSCI.2055-
1041 17.2017.

1042 Silva, J.D.N., Oliveira, L.M., Souza, F.C., Moreira, T.S., and Takakura, A.C. (2020). GABAergic
1043 neurons of the medullary raphe regulate active expiration during hypercapnia. J Neurophysiol *123*,
1044 1933-1943. 10.1152/jn.00698.2019.

1045 Silva, J.N., Oliveira, L.M., Souza, F.C., Moreira, T.S., and Takakura, A.C. (2019). Distinct
1046 pathways to the parafacial respiratory group to trigger active expiration in adult rats. American
1047 Journal of Physiology-Lung Cellular and Molecular Physiology *317*, L402-L413.
1048 10.1152/ajplung.00467.2018.

1049 Sobel, N., Prabhakaran, V., Desmond, J.E., Glover, G.H., Goode, R.L., Sullivan, E.V., and
1050 Gabrieli, J.D. (1998a). Sniffing and smelling: separate subsystems in the human olfactory cortex.
1051 Nature *392*, 282-286. 10.1038/32654.

1052 Sobel, N., Prabhakaran, V., Hartley, C.A., Desmond, J.E., Zhao, Z., Glover, G.H., Gabrieli, J.D.E.,
1053 and Sullivan, E.V. (1998b). Odorant-Induced and Sniff-Induced Activation in the Cerebellum of the
1054 Human. The Journal of Neuroscience *18*, 8990. 10.1523/JNEUROSCI.18-21-08990.1998.

1055 Souza, G., Kanbar, R., Stornetta, D.S., Abbott, S.B.G., Stornetta, R.L., and Guyenet, P.G. (2018).
1056 Breathing regulation and blood gas homeostasis after near complete lesions of the retrotrapezoid
1057 nucleus in adult rats. J Physiol *596*, 2521-2545. 10.1113/JP275866.

1058 Stornetta, R.L., Moreira, T.S., Takakura, A.C., Kang, B.J., Chang, D.A., West, G.H., Brunet, J.F.,
1059 Mulkey, D.K., Bayliss, D.A., and Guyenet, P.G. (2006). Expression of Phox2b by brainstem

neurons involved in chemosensory integration in the adult rat. J Neurosci *26*, 10305-10314. 26/40/10305 [pii]
10.1523/JNEUROSCI.2917-06.2006.

Stornetta, R.L., Spirovski, D., Moreira, T.S., Takakura, A.C., West, G.H., Gwilt, J.M., Pilowsky, P.M., and Guyenet, P.G. (2009). Galanin is a selective marker of the retrotrapezoid nucleus in rats. The Journal of comparative neurology *512*, 373-383. 10.1002/cne.21897.

Vallbo, A.B., and Johansson, R. (1984). Properties of cutaneous mechanoreceptors in the human hand related to touch sensation. Human neurobiology *3*, 3-14.

Vanderwolf, C.H. (2001). The hippocampus as an olfacto-motor mechanism: were the classical anatomists right after all? Behav. Brain Res. *127*, 25-47. 10.1016/s0166-4328(01)00354-0.

Veasey, S.C., Fornal, C.A., Metzler, C.W., and Jacobs, B.L. (1995). Response of serotonergic caudal raphe neurons in relation to specific motor activities in freely moving cats. J Neurosci *15*, 5346-5359.

Wang, S., Shi, Y., Shu, S., Guyenet, P.G., and Bayliss, D.A. (2013). Phox2b-expressing retrotrapezoid neurons are intrinsically responsive to H+ and CO2. J Neurosci *33*, 7756-7761. 10.1523/JNEUROSCI.5550-12.2013.

Widdicombe, J.G. (1954). Receptors in the trachea and bronchi of the cat. The Journal of physiology *123*, 71-104. 10.1113/jphysiol.1954.sp005034.

Yang, C.F., Kim, E.J., Callaway, E.M., and Feldman, J.L. (2019). Monosynaptic projections to excitatory and inhibitory preBötzinger Complex neurons. bioRxiv, 694711. 10.1101/694711.

Zhang, X.Y., Dou, Y.N., Yuan, L., Li, Q., Zhu, Y.J., Wang, M., and Sun, Y.G. (2020). Different neuronal populations mediate inflammatory pain analgesia by exogenous and endogenous opioids. eLife *9*. 10.7554/eLife.55289.

Zhong, W., Li, Y., Feng, Q., and Luo, M. (2017). Learning and Stress Shape the Reward Response Patterns of Serotonin Neurons. J Neurosci *37*, 8863-8875. 10.1523/jneurosci.1181-17.2017.

Ziv, Y., and Ghosh, K.K. (2015). Miniature microscopes for large-scale imaging of neuronal activity in freely behaving rodents. Curr Opin Neurobiol *32*, 141-147. 10.1016/j.conb.2015.04.001.

Zoccal, D.B., Silva, J.N., Barnett, W.H., Lemes, E.V., Falquetto, B., Colombari, E., Molkov, Y.I., Moreira, T.S., and Takakura, A.C. (2018). Interaction between the retrotrapezoid nucleus and the parafacial respiratory group to regulate active expiration and sympathetic activity in rats. Am J Physiol Lung Cell Mol Physiol *315*, L891-L909. 10.1152/ajplung.00011.2018.

1091
1092

Figures and Legends

Figure 1: Experimental approach and movement artefact. A) A CONSORT flow diagram for inclusion/exclusion of experiments and cells from the study. B) Representation of GRIN lens (microendoscope), baseplate, and mini epifluorescence camera placement for recording of brainstem nuclei. C-D) GFP control. RTN neurons were transduced with AAV-Syn-GFP (not Ca^{2+} sensitive) and GRIN lens implanted. Fluorescence was recorded going from 0 to 6% inspired CO_2 (gray bar). WBP: whole body plethysmography trace showing breathing movements. No signals are seen that resemble the Ca^{2+} transients observed with GCaMP6. E) Comparison of Ca^{2+} fluorescence signals observed with GCaMP6 versus movement from WBP trace (WBP sonogram) and head movement as observed from video recording (Mov sonogram). In expanded traces- a,b, Examples of lack of fluorescence signal during movement of head/body; c,f, examples of fluorescence signal in the absence of movement; d,e, examples of fluorescence signals during movement. (Scalebar- 20 μm) F) Seizures caused increase in activity of RTN neurons that was corelated with changes in breathing in anaesthetized mouse. Changes in mouse WBP before and after induction of non-behavioural seizures with intraperitoneal injection of kainic acid time matched with the activity of RTN neurons (red). The dotted square is changes in activity of neurons (ROIs) time matched with WBP and expanded in panel G. G) Increase in the activity of RTN neurons correlated with changes in breathing. The start of the GCaMP6 transient is shown by the dotted line. Ca^{2+} transients with a fast rise and exponential fall (pink traces); and slower sustained changes (turquoise traces).

Figure 2: Excitatory chemosensory responses of RTN neurons in awake mice. (A) AAV9-Syn-GCaMP6s injection into the RTN. B) Micrograph of lens placement and viral transduction of neurons (green) relative to the facial nucleus (ChAT+ neurons - red). C) Venn diagram of cell counts of GCaMP6s transduced (green), and ChAT+ (red), neurons under the GRIN lens (1 representative section from each of 4 mice). D) Neurons transduced with GCaMP6s also contain NMB confirming their identity as RTN neurons. E) Venn diagram of cell counts of GCaMP6s transduced (green), and NMB+ (magenta), neurons under the GRIN lens (1 representative section from each of 3 mice). F) Recording of mouse whole body plethysmography (WBP) in response to hypercapnia time-matched with Inscopix recorded GCaMP6 signals. These show neurons that gave a graded response to CO_2 (E_G). G) Average of the graded neuronal responses aligned to the WBP trace in F). H) Examples of neurons that showed an adapting response to a change in inspired CO_2 (E_A). WBP trace aligned to the GCaMP6 fluorescence and instantaneous V_E (minute ventilation) shown to demonstrate how the signals in the E_A neurons closely correspond to V_E. I) Average waveform of all E_A neurons in the RTN aligned to 0, 3 and 6% inspired CO_2 (gray bar). J) A plot of V_T versus F/F0 for the Ca^{2+} signal during the transition from 0 to 3% CO_2 in three individual mice showing positive correlation. Underneath each V_T vs F/F0 graph is a plot of change

in V_T (grey) and average of E_A neuronal Ca^{2+} activity (magenta) from respective mouse during transition from baseline to 3% CO_2. Note that there is a transient increase in breathing at the beginning of hypercapnia that corresponds to the activation of the E_A neurons.
Abbreviations: 7N, facial motor nucleus; Py, pyramidal tract; MVe, medial vestibular nucleus; sp5, spinal trigeminal nucleus: RTN, retrotrapezoid nucleus; RMg, raphe magnus; RPa, raphe pallidus; pF_L, parafacial lateral region.

Figure 3: Sniff-coding, and CO_2-inhibited RTN neuronal responses in awake mice. (A) Recording of mouse WBP in response to hypercapnia time-matched with Inscopix recorded GCaMP6 signals. CO_2-Inhibited (blue) and sniff-coding (eggplant purple) calcium traces correspond to the neurons shown in panel F. (B) Expanded recordings from (A), the start of the Ca^{2+} transient is shown by the dotted line. (C) Average waveform of RTN inhibited neurons in response to hypercapnia. (D) Sniff-correlation histogram and (E) Spike triggered average (eggplant purple line) of all Ca^{2+} events (grey lines) temporally correlated to the beginning of sniff activity (dotted verticle line). (F) GCaMP6s fluorescence of transduced RTN neurons in freely behaving mice. Individual regions of interest (ROIs) drawn around CO_2-inhibited (blue) and sniff coactivated (eggplant purple) neurons. (Scalebar- 20 μm).

Figure 4: Tonically active, non-coding (NC) and NC-respiratory related (NC-RR) RTN neuronal responses in awake mice. Recording of mouse WBP in response to hypercapnia time-matched with Inscopix recorded GCaMP6 signals (A, B, C). GCaMP fluorescence of RTN (A) tonically active (T; violet blue) (B) non-coding (NC; green) and (C) non-coding respiratory related (NC-RR; shamrock green) neurons. Average of NC-RR neuronal activity (dotted box) expanded under it displayed Ca^{2+} signals that were correlated to changes in respiratory frequency (*f*R) and were generally silent when tidal volume (WBP) was at its greatest.

Figure 5: CO_2-excitated medullary raphe neurons in awake mice. (A) AAV injection into the Raphe. (B) Micrograph of lens placement and AAV9-Syn-GCaMP6s viral transduction of neurons (green) relative to the Raphe (TPH+ neurons - red). (C) GCaMP6s fluorescence signal from AAV9-Syn-GCaMP6s transduced raphe neurons in freely behaving mice (Scale bar- 50 μm). (D) Venn diagram of cell counts of AAV9-Syn-GCaMP6s transduced neurons (green) under the GRIN lens with TPH+ neurons (red) in the raphe (1 representative section from each of 4 mice). (E) Micrograph of lens placement and AAV9-SERT-GCaMP6s viral transduction of neurons (green) relative to the Raphe (TPH+ neurons - red). (F) GCaMP6s fluorescence signal from AAV9-SERT-GCaMP6s transduced raphe neurons in freely behaving mice (Scale bar- 50 μm). (G) WBP recording in response to hypercapnia time-matched with Inscopix recorded GCaMP6 signals. GCaMP fluorescence of raphe excitatory graded (E_G), and excitatory adapting (E_A) neurons in

response to hypercapnia. (H-I) Average waveform of raphe E_G neuronal responses to hypercapnia aligned to the WBP trace in G. Abbreviations defined in Figure 2.

Figure 6. CO_2-inhibited and non-coding raphe neuronal responses in awake mice. Recording of mouse WBP in response to hypercapnia time-matched with Inscopix recorded GCaMP6 signals. GCaMP fluorescence of raphe CO_2 inhibited (I; blue) (A) and non-coding (NC; green) (C) neurons. (B) Average waveform of raphe inhibited neurons in response to hypercapnia aligned to the WBP trace in A.

Figure 7: pF_L neurons drive active expiration. (A) AAV9-Syn-GCaMP6f injection into the pF_L. (B) Micrograph of lens placement and viral transduction of pF_L neurons (green) relative to the facial nucleus (ChAT+ neurons - red). (C) GCaMP6f fluorescence signal from transduced pF_L neurons in freely behaving mice (Scale bar- 50 µm). (D) Venn diagram of cell counts of GCaMP6f transduced (green) and ChAT+ (red) neurons under the GRIN lens (1 representative section from each of 3 mice). (E) Movement artefact subtracted from GCaMP signal extracts a clear Ca^{2+} transient from pF_L neurons. An ROI was placed over the border of a blood vessel (background/movement; black) and the subsequent fluoresence recording was subtracted from the GCaMP signal (uncorrected GCaMP; red) giving rise to neuronal Ca^{2+} transients of pF_L neurons (corrected GCaMP; green) in awake mice that are free from the movement artefact. (F) WBP recording in response to hypercapnia time-matched with Inscopix recorded GCaMP signals. GCaMP6f fluorescence of transient expiratory (Exp; dark brown) pF_L neurons. (G) Expanded traces from (F), the start of the Ca^{2+} transient is shown by the brown dotted line. (H) Measurements of GCaMP6 fluorescence (dark brown) relative to tidal volume (V_T, blue), respiratory frequency (*f*R, grey), and expiration (Exp, red). Verticle dotted lines represent the start of the changes on their respective channels. (I-K) Frequency histograms of timing of changes in GCaMP fluorescence of pF_L neurons relative to tidal volume (V_T, left), respiratory frequency (*f*R, centre), and expiration (Exp, right). (L-M) Spike triggered average (brown line) of all Ca^{2+} events (grey lines) temporally correlated to the beginning of expiratory activity (dotted verticle line) at (L) 6% CO_2 and (M) 9% CO_2. Abbreviations defined in Figure 2.

Figure 8. Summary diagram of findings in the paper showing contribution of the RTN, Raphe and pF_L neurons to respiratory chemosensitivity and active expiration. A) Block diagram showing the types of activity pattern observed in neurons of the RTN, pF_L and Raphe. Proposed potential interconnections to the preBötzinger and Bötzinger complexes are speculative and based on regional interactions reported in the literature. B) Hypothesis for generating CO_2

dependent inhibition of serotonergic neurons. CO_2 is proposed to activate GABAergic neurons that inhibit tonically active serotonergic neurons which are not directly CO_2 sensitive. If these were to activate a separate population of non-CO_2 sensitive GABAergic neurons, these could normally silence the CO_2 sensitive neurons until an episode of hypercapnia. This mechanism could explain an indirect inhibitory action of CO_2 on both serotonergic and GABAergic neurons. C) Averages of the different types of neuronal activity seen in the RTN, Raphe and pF_L during hypercapnia aligned to an average of the WBP trace.

Figure 1 Supplement Figure 1: The depth of focus of the GRIN lens. The focal plane and depth of GRIN lens from the fluorescent beads when camera turret was at the maximum (4 turns) high and at maximum low (0 turns) positions.

Figure 1 Figure Supplement 2: All RTN neurons responses to the hypercapnic challenge. RTN excited graded (E_G), excited adapting (E_A), inhibited (I), sniff-coding (Sn), non-coding (NC), tonically active (T), and non-coding respiratory related (NC-RR) neuronal responses time-matched with hypercapnia (light grey-3% CO_2, medium grey-6% CO_2) and average waveforms of E_G, E_A, and I. Animal number is mentioned on the left hand side of the neuronal trace and camera turret position on the right hand side of the neuronal traces. All recordings of neuronal activity from a particular mouse are taken from the same imaging session for that mouse.

Figure 1 Figure Supplement 3: All raphe neurons responses to the hypercapnic challenge. Raphe excited graded (E_G), excited adapting (E_A), inhibited (I), and non-coding (NC) neuronal responses time-matched with hypercapnia (light grey-3% CO_2, medium grey-6% CO_2), and average waveforms of E_G, E_A, and I. Animal number is indicated on the left hand side of the neuronal trace, and neuronal promoter and camera turret position on the right hand side of the neuronal traces. All recordings of neuronal activity from a particular mouse are taken from the same imaging session for that mouse.

Figure 1 Figure Supplement 4: All pF_L neuronal responses to the hypercapnic challenge (medium grey-6% CO_2, dark grey-9% CO_2). Animal number is indicated on the left hand side of the neuronal trace and camera turret position on the right hand side of the neuronal traces. All recordings of neuronal activity from a particular mouse are taken from the same imaging session for that mouse.

Figure 1 Figure Supplement 5: Consistent responses to hypercapnia in RTN neurons were recorded between sessions from the same mouse. Session-A represents the recordings that contribute to the RTN neuronal dataset in Figure 1 Figure Supplement 2. Session-B represents recordings from a different session from the same mice. These recordings are not included in the dataset to avoid pseudoreplication but show that the same types of neuronal responses were consistently observed between sessions.

Figure 1 Figure Supplement 6: Activity patterns of individual RTN neurons remains very similar across recording sessions. Left and right panels are different recordings sessions of the same neurons identified between different recording sessions from the same mouse on different days. The numbers represent neuron identification.

Figure 1 Figure Supplement 7: Two component analysis of neuronal categorisation in Raphe and RTN nuclei. The change in Ca^{2+} signal (measured as area under the curve) from baseline (room air) elicited by 6% CO_2 plotted against the Ca^{2+} response elicited by 3% CO_2. The line of identity (x=y) is shown. E_A neurons fall below this line, whereas E_G neurons fall above this line. *NC* neurons are clustered around the origin (shown only for the RTN nucleus) and *I* neurons are predominantly in the negative quadrant of the graph.

Figure 1 Figure Supplement 7: Source Data 1

Figure 2 Figure Supplement 1: Validation of NMB immunostaining patterns. A) Section of caudal medulla oblongata, showing *in situ* hybridization (ISH) for NMB from the Allen Mouse Brain Atlas (mouse.brain-map.org/experiment/show/71836874) and equivalent section from the Allen Reference Atlas (atlas.brain-map.org): AP, area postrema; c, central canal; XII Hypoglossal nucleus; mlf, Medial longitudinal fascicle; DMX, Dorsal motor nucleus of the vagus nerve; sptV, Spinal tract of the trigeminal nerve. B) NMB immunostaining of equivalent section to A and ChAT staining in the same section showing localisation of XII. Bi and Bii high resolution images of the boxes in B showing presence of NMB immunoreactivity corresponding to the ISH above.

C) Section of caudal medulla oblongata, showing *in situ* hybridization (ISH) for NMB from the Allen Brain Atlas (mouse.brain-map.org/experiment/show/ 71836874) alongside the equivalent section from the Allen Reference Atlas (atlas.brain-map.org): abbreviations as in A; GR gracile nucleus; grf

gracile fascicle; MDRNvp Medullary reticular nucleus ventral part. D) NMB immunostaining showing equivalent section to the adjacent Allen Brain ISH section and ChAT in the same section showing localisation of XII. Di and Dii high resolution images of the boxes in the image to the left showing absence of NMB immunoreactivity in the mlf, corresponding to the ISH above. Note the absence of NMB staining in the mlf, and presence of NMB staining in the MDRNvp.

E) Section of forebrain, showing *in situ* hybridization (ISH) for NMB from the Allen Brain Atlas (mouse.brain-map.org/experiment/show/ 71836874) alongside the equivalent section from the Allen Reference Atlas (atlas.brain-map.org). Ei, Comparison of NMB staining in cortex with ISH from the Allen Brain Atlas at a corresponding location. Note the absence of NMB staining in cortical layer 1, and sporadic staining for NMB in deeper layers, which matches the ISH pattern. Eii, NMB staining in the dentate gyrus corresponds with ISH from the Allen Brain Atlas. Eiii, NMB staining in the piriform and amygdalar cortex, note its absence in the superficial layers corresponds to the absence of ISH in the equivalent Allen Brain image.

Figure 2 -figure supplement 2: The dynamics of individual Ca^{2+} transients from two E_A cells and two T cells recorded in the RTN before, during and after hypercapnia. Individual transients (denoted by boxes in continuous trace) have been scaled, aligned to the decay phase and superimposed to show that the decay phase (reflecting extrusion/sequestration) remains constant and longer in duration than the rising phase (reflecting influx) during the entire experiment. Note that neither the decay phase nor the rising phase show any notable changes that could account for the adapting pattern of Ca^{2+} activity observed in the E_A cells.

Supplementary File 1: A user-modifiable worksheet that uses simple mathematical functions to explore the predicted correlation between V_T and F/F_0 for E_A neurons under two assumptions -i) no adapting component in the V_T response to hypercapnia; and ii) an adapting V_T component in the response to hypercapnia is present. This should be compared to the data shown in Figure 2J.

Figure 3 Source Data 1: Data for Figure 3 panels D and E.

Figure 4 Figure Supplement 1: Hypercapnia induced RTN neuronal responses in awake and anesthesized mice. A-B) Successive recordings from the same cells under the awake and anaesthesia states. Note how anaesthesia reduces the spontaneous activity of the neurons relative to the awake state. Under anaesthesia neurons are completely silent (A-B). (C) In two different mice (top and bottom) recorded under awake and anaesthesia at different sessions, the same cells showed completely different responses under these awake and anaesthesia states.

Note how cells displaying a graded response to hypercapnia under anaesthesia were classified as non-coding respiratory related (NC-RR) or non-coding (NC) in the awake state.

Figure 4 Figure Supplement 2: Change in breathing frequency (*f*R), tidal volume (V_T) and minute ventilation (V_E) in response hypercapnia from mice recorded in the study. Change in tidal volume (V_T; left) breathing frequency (*f*R, bpm; centre), and minute ventilation (V_E; right) in response to changes in CO_2 concentration in mice from which (A) RTN neurons, (B) Raphe neurons, (C) pF_L neurons were recorded.

Figure 4 Figure Supplement 2 Source Data 1: Data for Figure 4 Figure Supplement 2.

Figure 7 Source Data 1: Data for Figure 7 panels I-K.

Figure 1-Video 1: RTN neuronal responses to hypercapnia in mice transfected with synapsin GFP control (without GCaMP).

Figure 1-Video 2: Mouse undergoing kainate induced electrographic seizures in absence of physical seizures.

Figure 2-Video 1: Excited graded (E_G) RTN neuronal response to hypercapnia in synapsin GCaMP6 transfected mice.

Figure 2-Video 2: Excited adapting (E_A) RTN neuronal response to hypercapnia in synapsin GCaMP6 transfected mice.

Figure 3-Video 1: RTN sniff-coding (Sn) and inhibited (I) neuronal responses in mice transduced with synapsin GCaMP6.

Figure 4-Video 1: Tonically active (T) RTN neurons (irrespective of hypercapnia) in synapsin GCaMP6 transfected mice.

Figure 5-Video 1: Excited graded (E_G) and adapting (E_A) Raphe neuronal responses to hypercapnia in synapsin GCaMP6 transfected mice.

Figure 6-Video 1: Inhibited Raphe neurons due to hypercapnia in SERT GCaMP6 transfected mice.

A

28 Mice assessed for eligibility
14 RTN Syn, 4 Raphe Syn,
6 Raphe SERT, and 4 pFL Syn

10 Mice excluded (5 RTN Syn,
2 Raphe Syn, 2 Raphe SERT,
and 1 pF_L Syn)
3 No Ca^{2+} signal
5 Low fluorescence (signal/noise)
2 Incorrect lens placement

194 Cells included for analysis

122 RTN neurons assessed for eligibility

14 Raphe Syn and
27 Raphe SERT neurons
assessed for eligibility

31 pF_L neurons assessed for eligibility

98 cells included.
0 excluded for no change in Ca^{2+} signal & 24 for movement artefact

26 cells included.
1 (Syn) excluded for no change in Ca^{2+} signal & 4 Syn & 10 SERT for movement artefact

20 cells included.
5 excluded for no change in Ca^{2+} signal & 6 for movement artefact

B

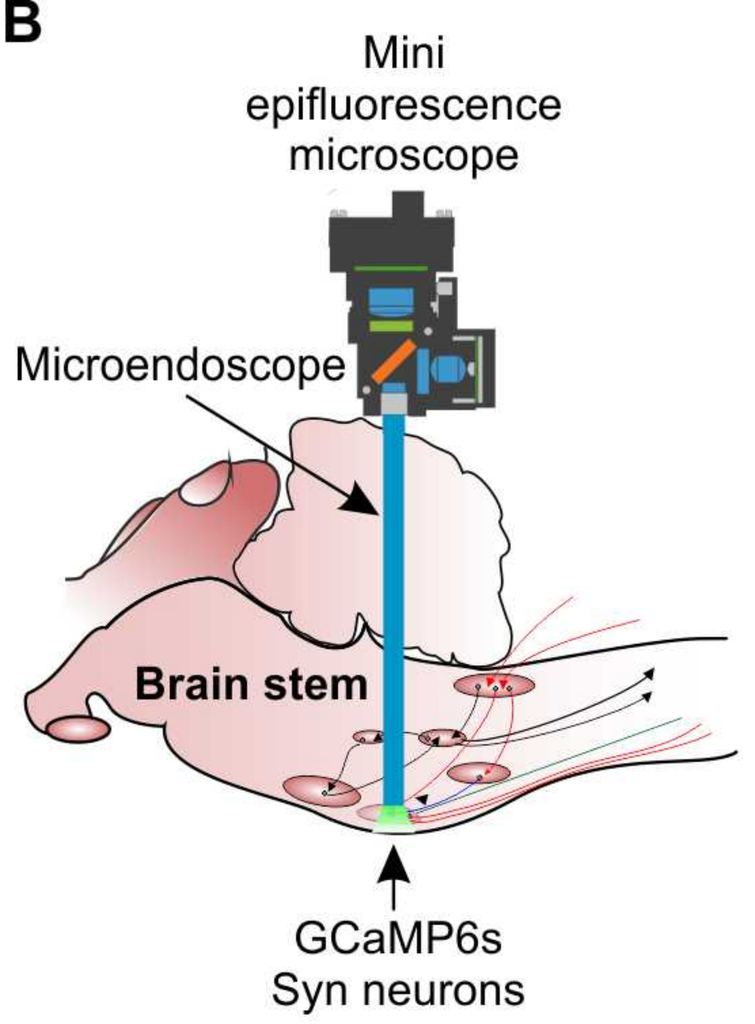

C

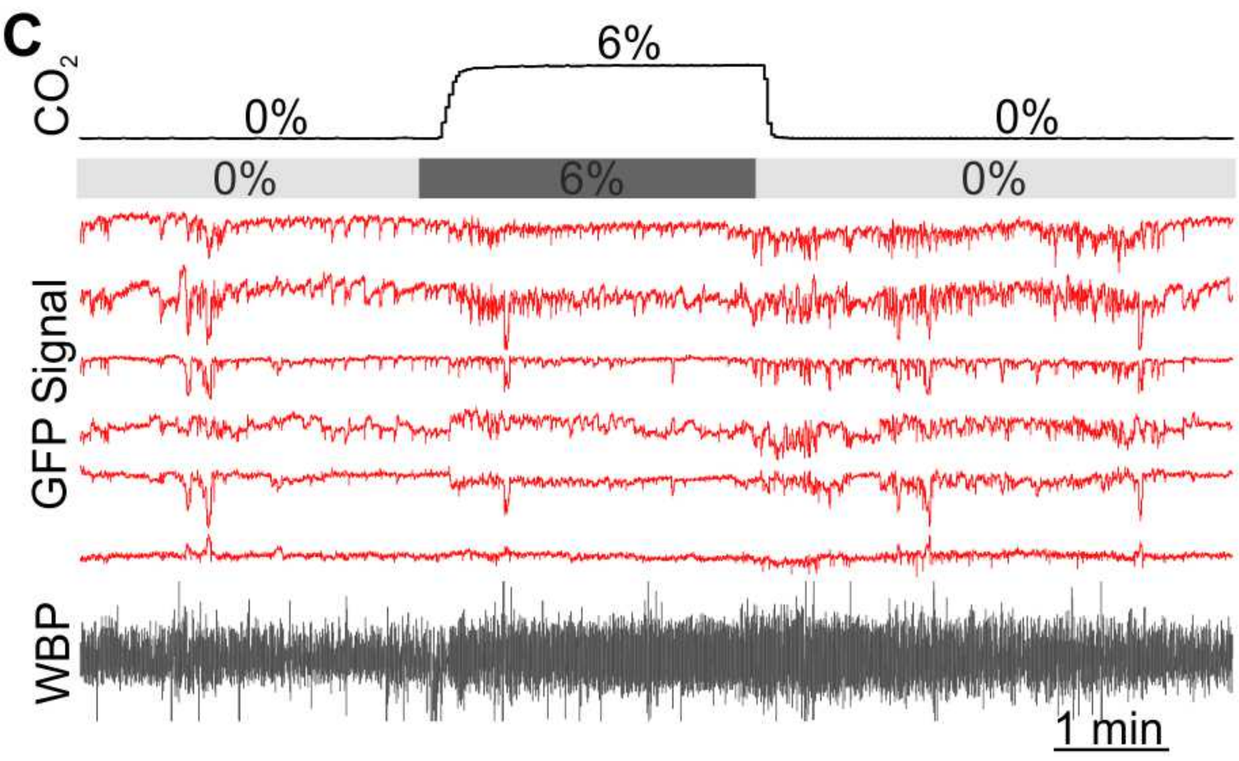

D

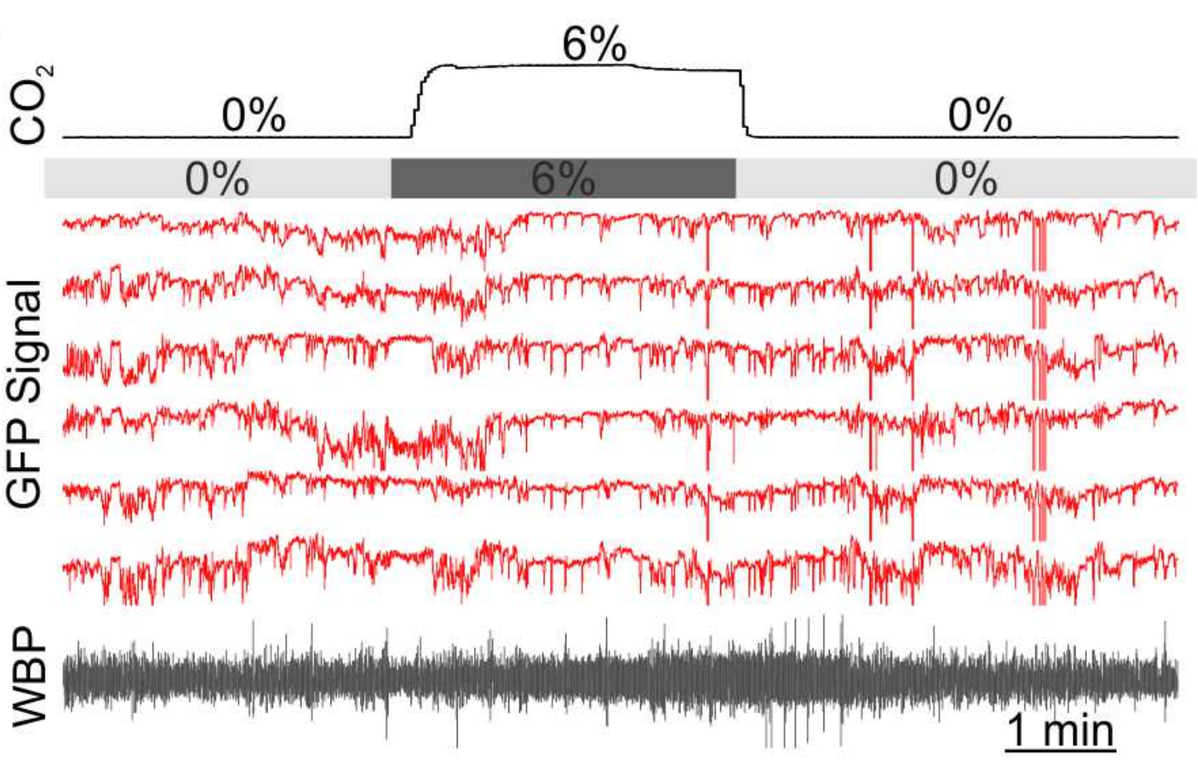

E

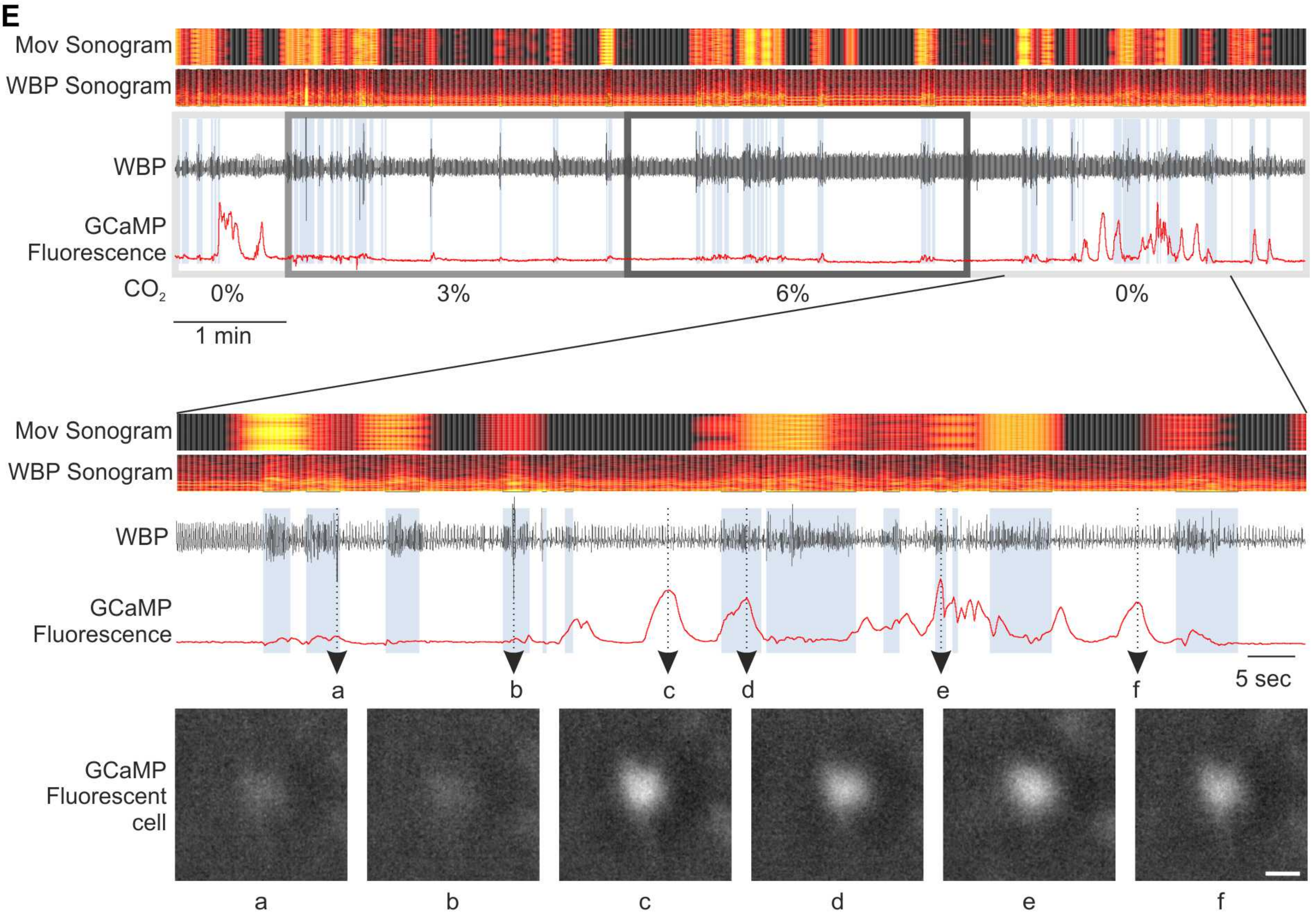

F

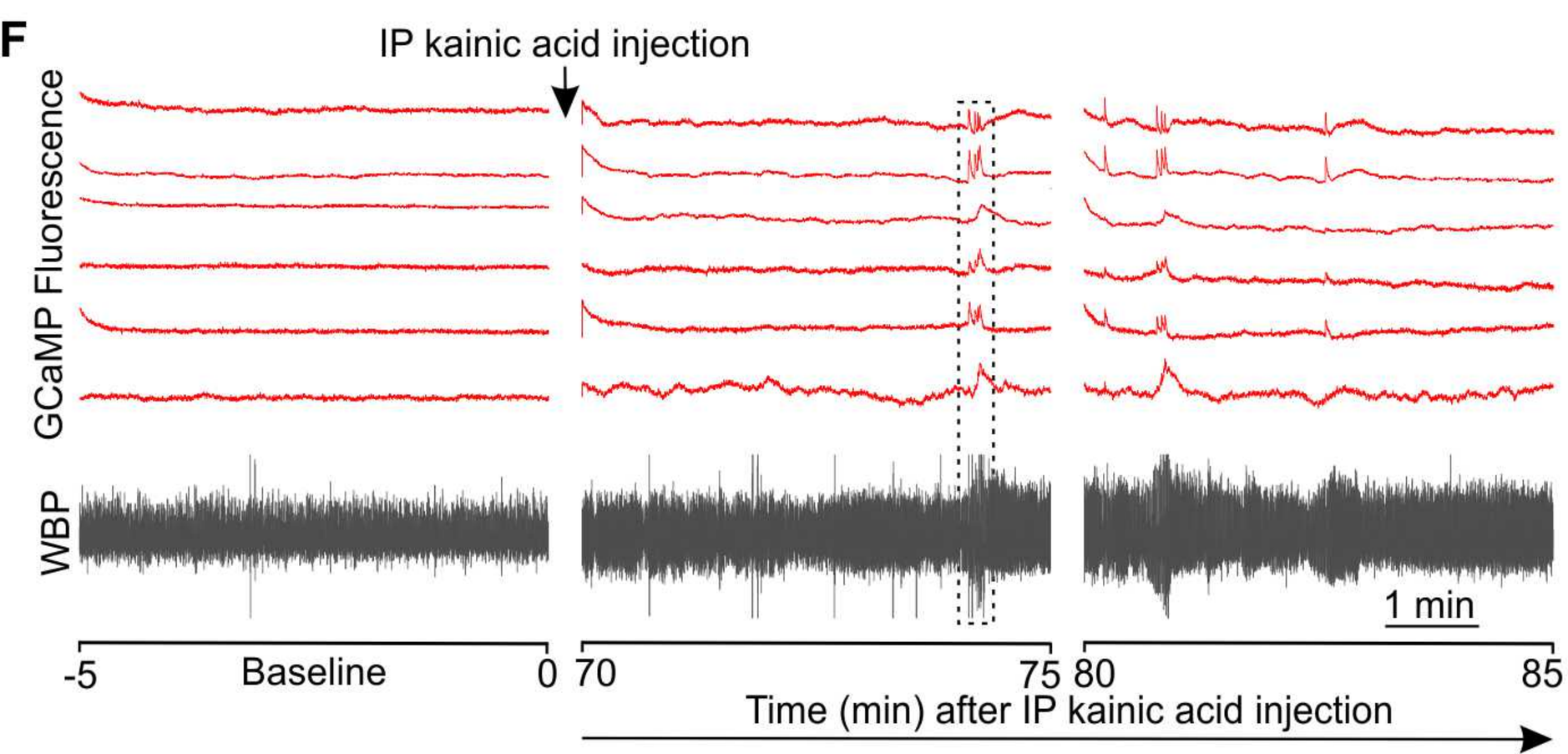

G

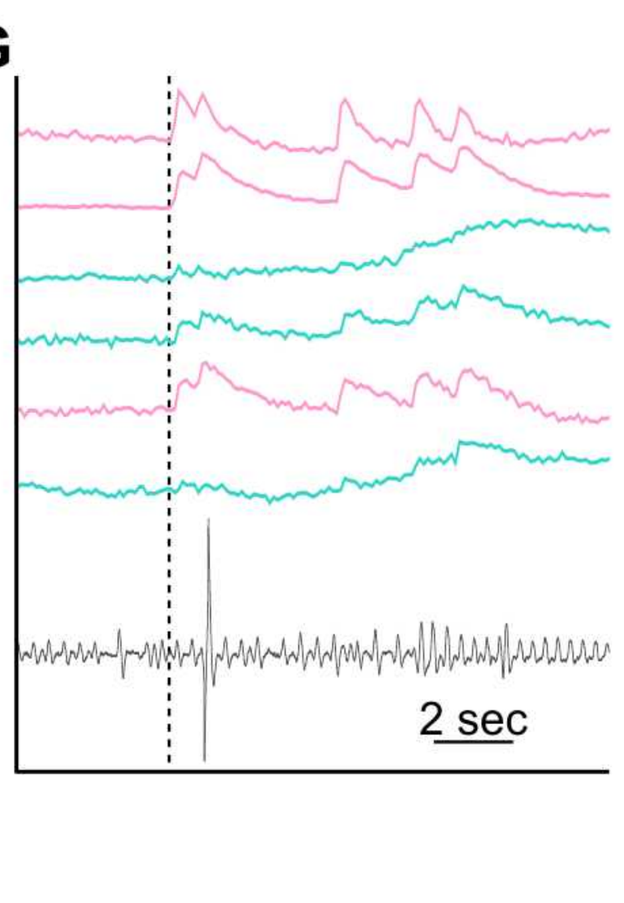

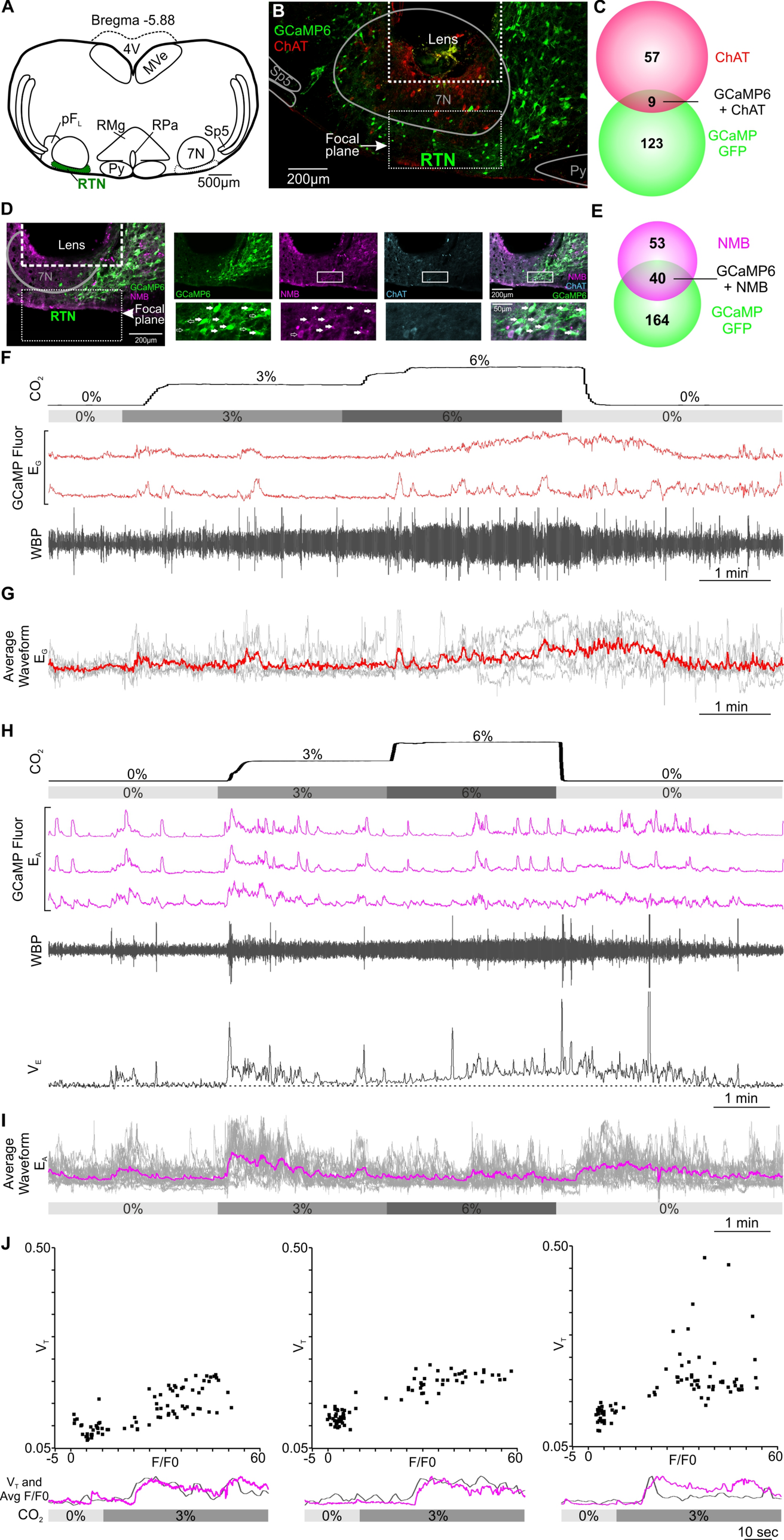
A
Bregma -5.88
4V
MVe
pF_L
RMg
RPa
Sp5
7N
Py
RTN
500µm
B
GCaMP6
ChAT
Lens
Sp5
7N
Focal plane
RTN
Py
200µm
C
57
ChAT
9
GCaMP6 + ChAT
123
GCaMP GFP
D
Lens
7N
GCaMP6
NMB
RTN
Focal plane
200µm
GCaMP6
NMB
ChAT
NMB
ChAT
GCaMP6
200µm
50µm
E
53
NMB
40
GCaMP6 + NMB
164
GCaMP GFP
F
CO2
0%
3%
6%
0%
0%
3%
6%
0%
GCaMP Fluor
E_G
WBP
1 min
G
Average Waveform
E_G
1 min
H
CO2
0%
3%
6%
0%
0%
3%
6%
0%
GCaMP Fluor
E_A
WBP
V_E
1 min
I
Average Waveform
E_A
0%
3%
6%
0%
1 min
J
0.50
0.05
V_T
-5
0
F/F0
60
V_T and Avg F/F0
CO2
0%
3%
10 sec

A

CO_2

0%

3%

6%

0%

0%

3%

6%

0%

GCaMP Fluorescence

I

Sn

WBP

a

b

c

d

e

f

g

h

1 min

B

a

b

c

d

e

f

g

h

2 sec

C

Average Waveform

I

0%

3%

6%

0%

1 min

D

10

f

-1.6

-1.2

-0.8

-0.4

0

0.4

0.8

1.2

1.6

Time relative to change (s)

E

GCaMP Fluorescence

-5

0

5

Time (s) relative to sniff

F

RTN Syn GCaMP cells

A

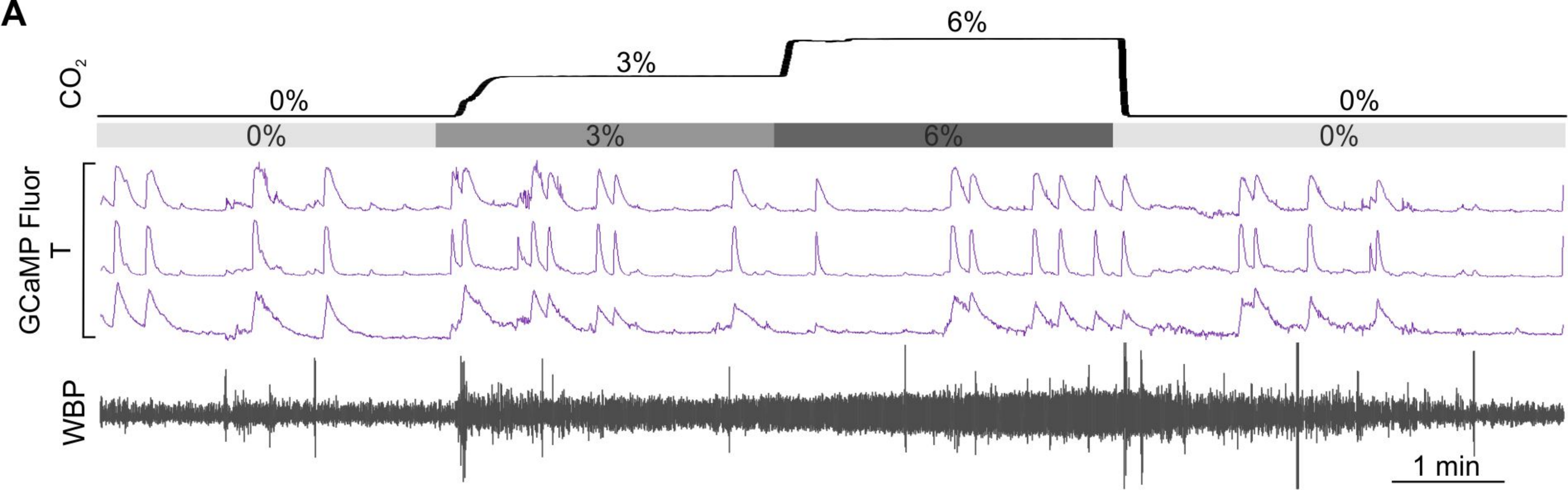
CO_2
0%
3%
6%
0%
0%
3%
6%
0%
GCaMP Fluor T
WBP
1 min

B

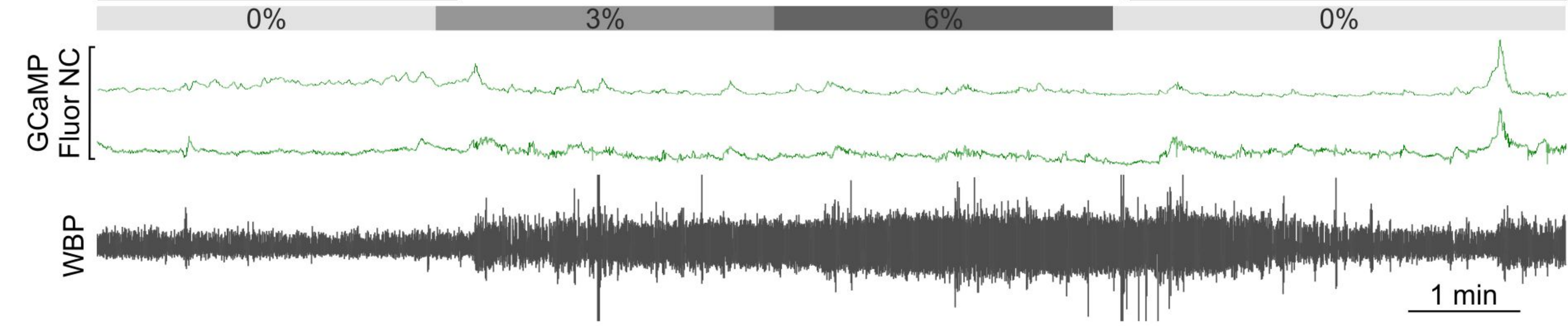
CO_2
0%
3%
6%
0%
0%
3%
6%
0%
GCaMP Fluor NC
WBP
1 min

C

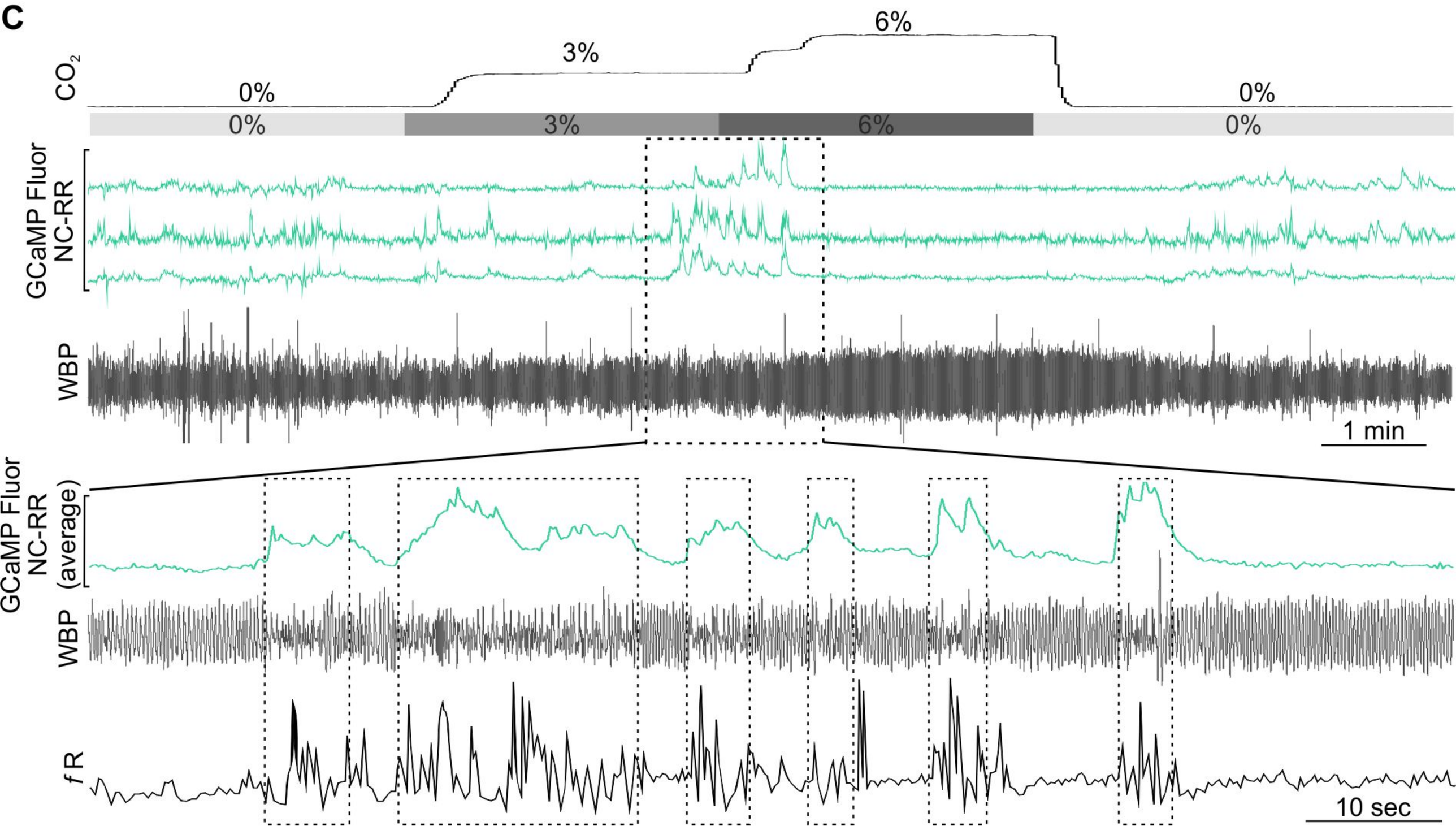
CO_2
0%
3%
6%
0%
0%
3%
6%
0%
GCaMP Fluor NC-RR
WBP
1 min
GCaMP Fluor NC-RR (average)
WBP
fR
10 sec

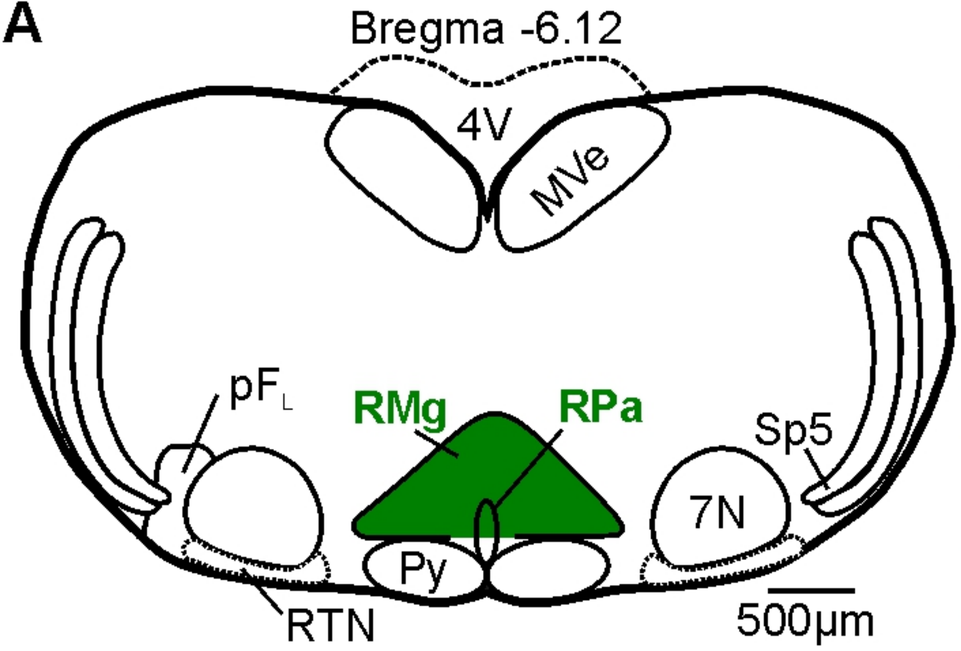
A
Bregma -6.12
4V
MVe
pF_L
RMg
RPa
Sp5
7N
Py
RTN
500µm

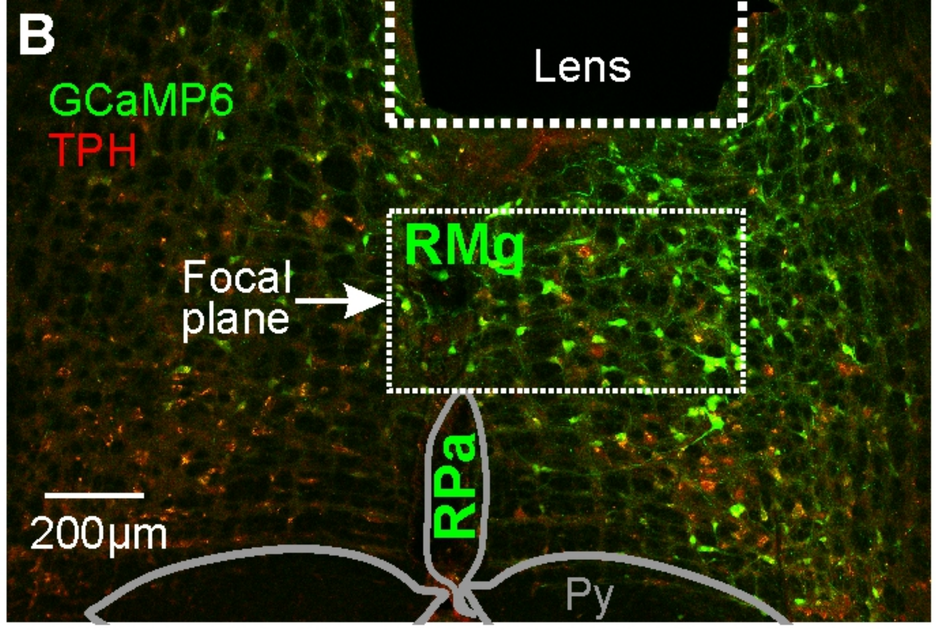
B
GCaMP6
TPH
Lens
RMg
Focal
plane
RPa
200µm
Py

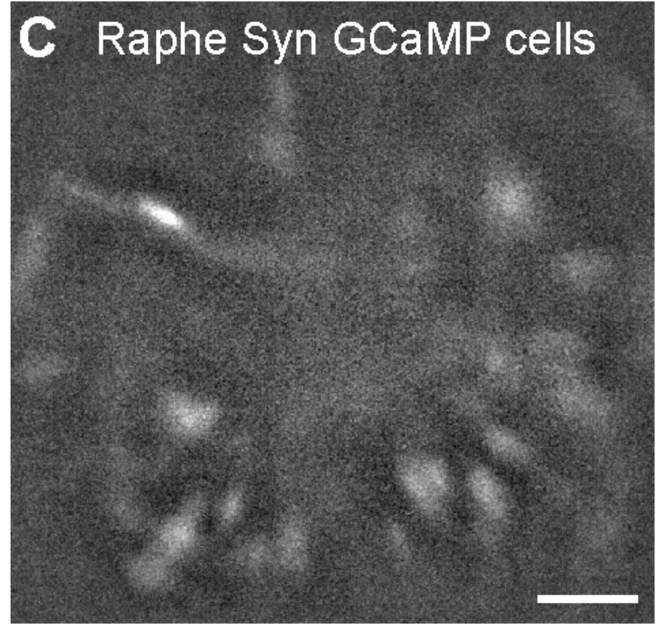
C
Raphe Syn GCaMP cells

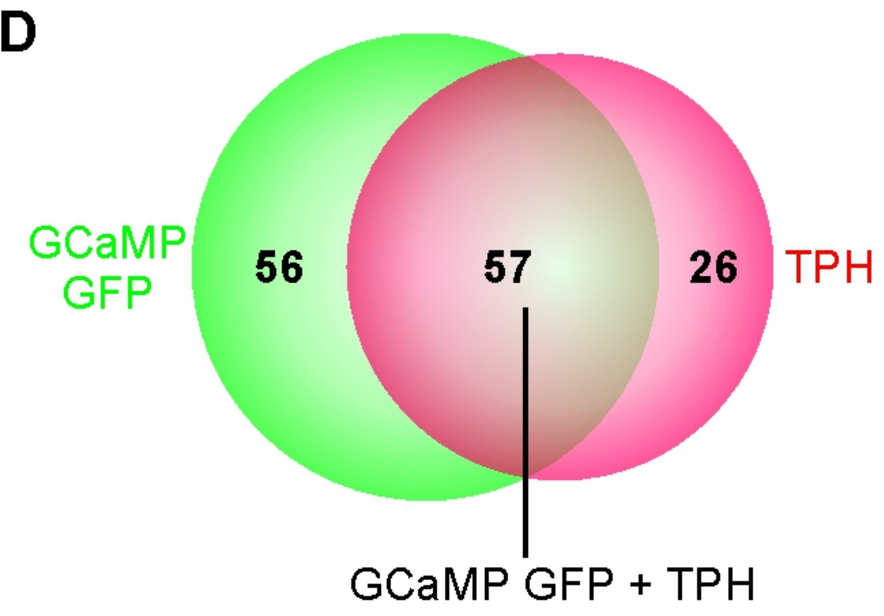
D
GCaMP
GFP
56
57
26
TPH
GCaMP GFP + TPH

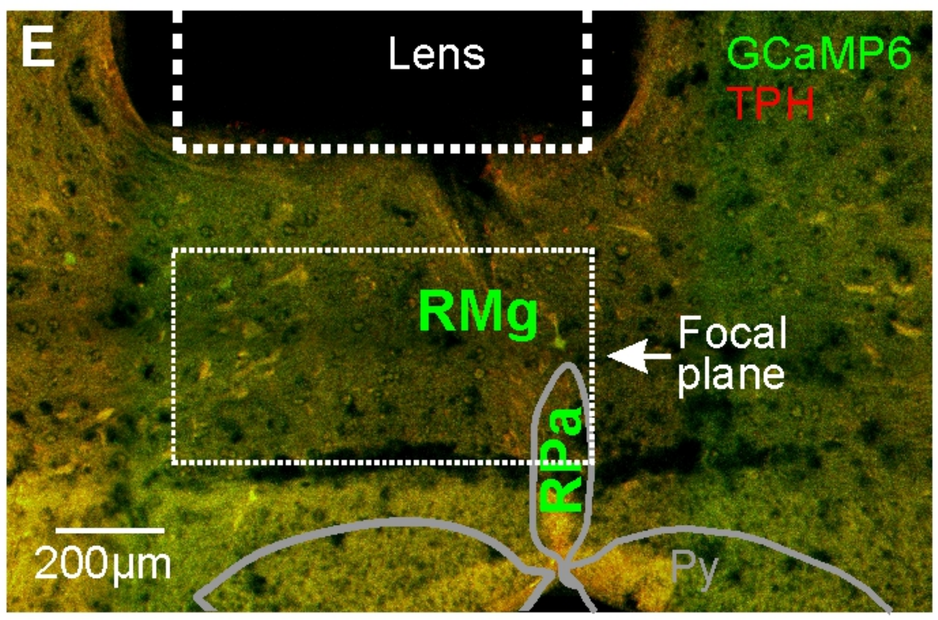
E
Lens
GCaMP6
TPH
RMg
Focal
plane
RPa
200µm
Py

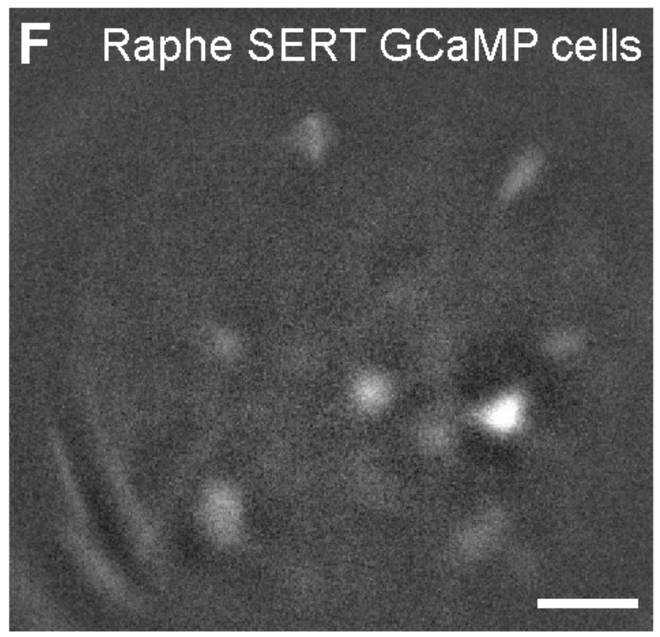
F
Raphe SERT GCaMP cells

G
CO2
0%
3%
6%
0%
0%
3%
6%
0%
GCaMP Fluorescence
E_G
E_A
WBP
1 min
H
Average
Waveform
E_G
1 min

A

CO_2

0%

3%

6%

0%

0%

3%

6%

0%

GCaMP Fluor I

WBP

1 min

B

Average Waveform

1 min

C

CO_2

0%

3%

6%

0%

0%

3%

6%

0%

GCaMP Fluor NC

WBP

1 min

A
Bregma -5.88
4V
MVe
pF$_L$
RMg
Rpa
Sp5
7N
Py
RTN
500µm
B
GCaMP
ChAT
Lens
Sp5
Focal plane
pF$_L$
7N
200 µm
C
pF$_L$ Syn GCaMP cells
D
GCaMP GFP
ChAT
69
2
58
E
Corrected GCaMP
GCaMP
Background /movement
20 sec
F
CO$_2$
0%
6%
9%
0%
0%
3%
6%
0%
GCaMP Fluor
*f*R
WBP
a
b
c
1 min
G
a
b
c
H
Δt *f*R
Δt Exp
Δt V$_T$
GCaMP
*f*R
Exp
V$_T$
WBP
2 sec
I
60
6 % CO$_2$
9 % CO$_2$
V$_T$
Count
0
-3
-2
-1
0
1
Time relative to change (s)
J
36
*f*R
Count
0
-3
-2
-1
0
1
Time relative to change (s)
K
36
Exp
Count
0
-1.6
-1.2
-0.8
-0.4
0
Time relative to change (s)
L
6% CO$_2$
GCaMP Fluorescence
-1
0
1
2
Time relative to Exp (s)
M
9% CO$_2$
GCaMP Fluorescence
-1
0
1
2
Time relative to Exp (s)

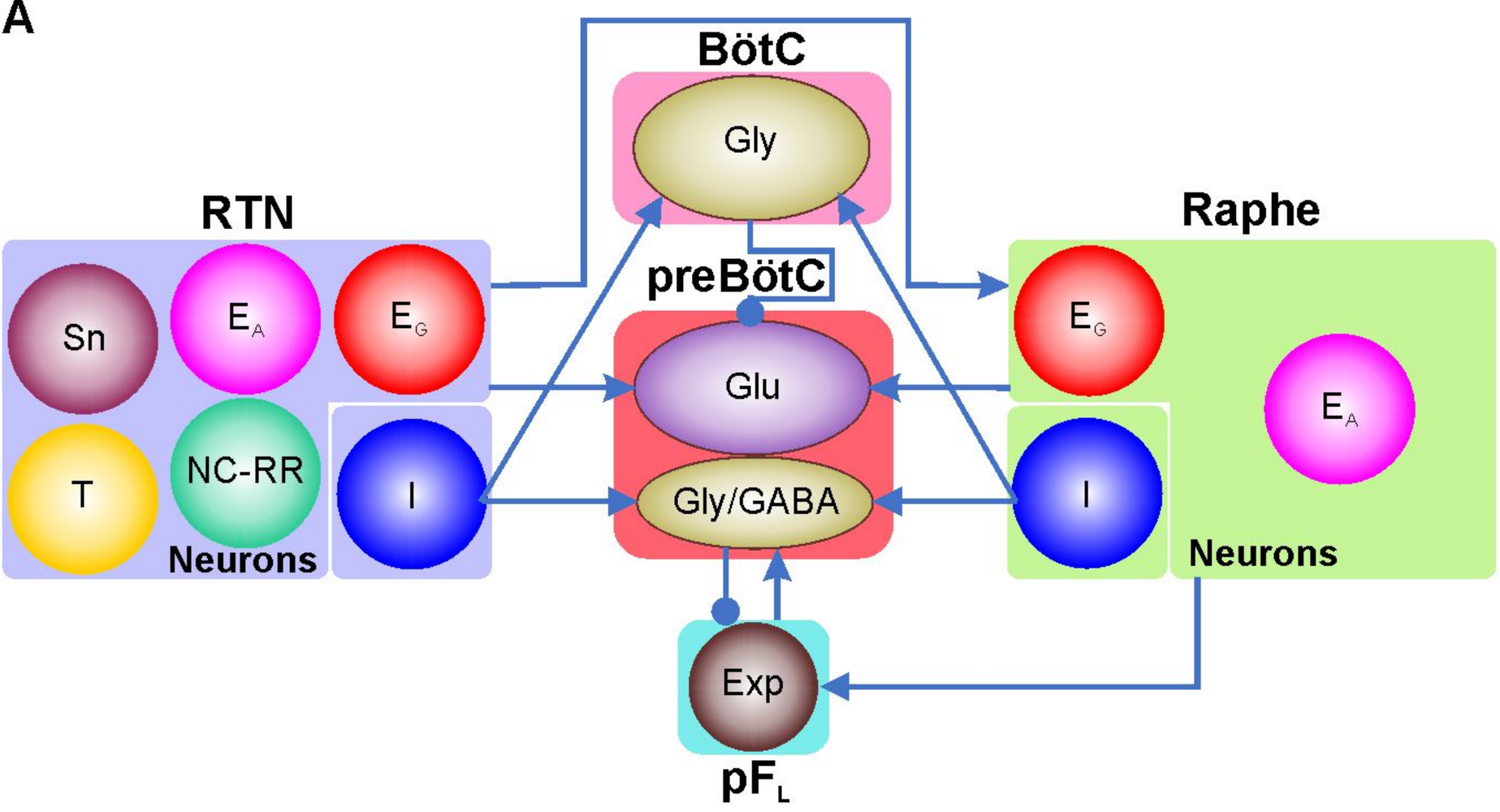
A
BötC
Gly
RTN
Raphe
preBötC
Sn
E_A
E_G
Glu
E_G
E_A
T
NC-RR
I
Gly/GABA
I
Neurons
Neurons
Exp
pF_L

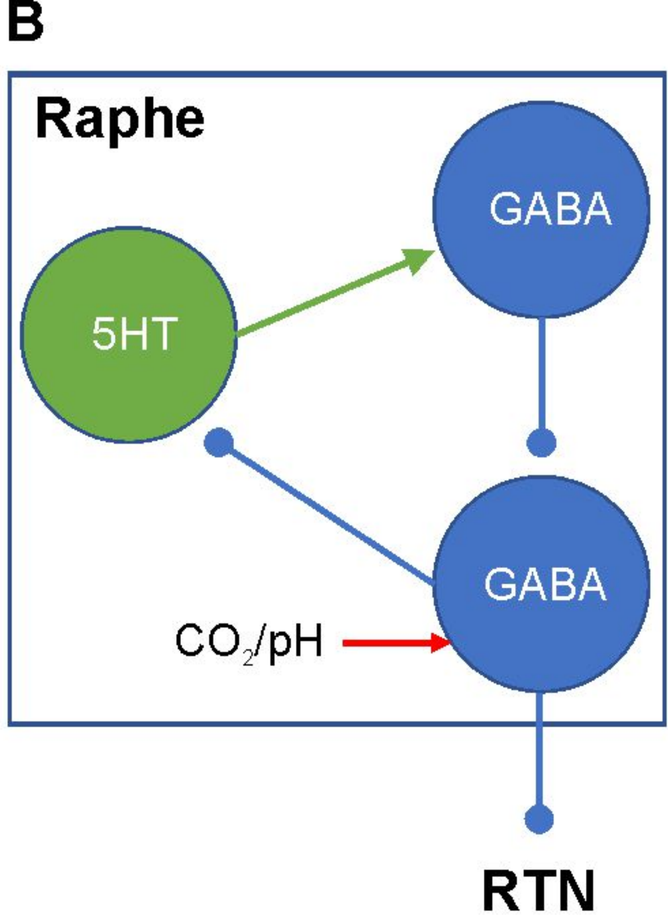
B
Raphe
GABA
5HT
GABA
CO2/pH
RTN

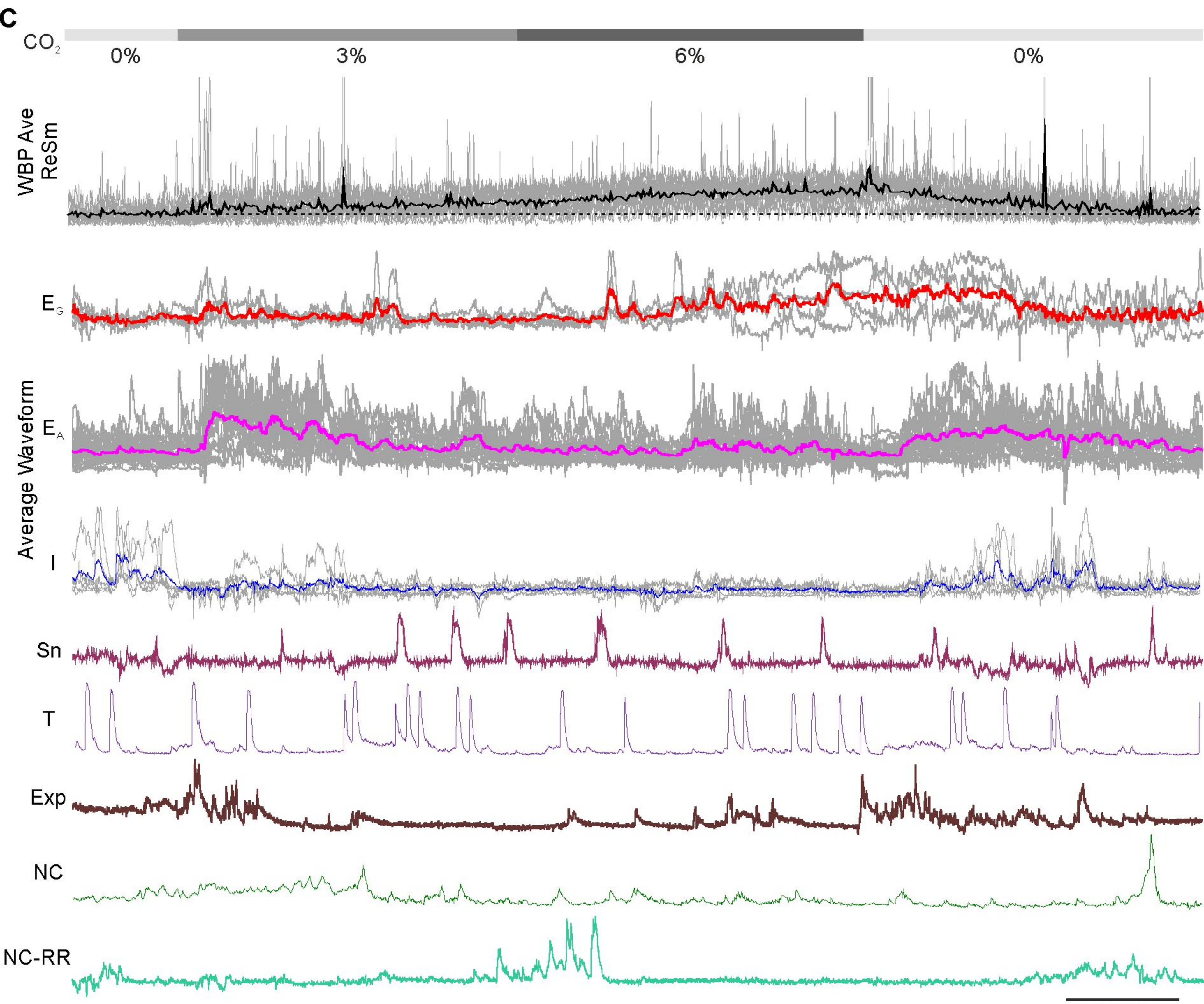
C
CO2
0%
3%
6%
0%
WBP Ave ReSm
E_G
E_A
Average Waveform
I
Sn
T
Exp
NC
NC-RR
1 min

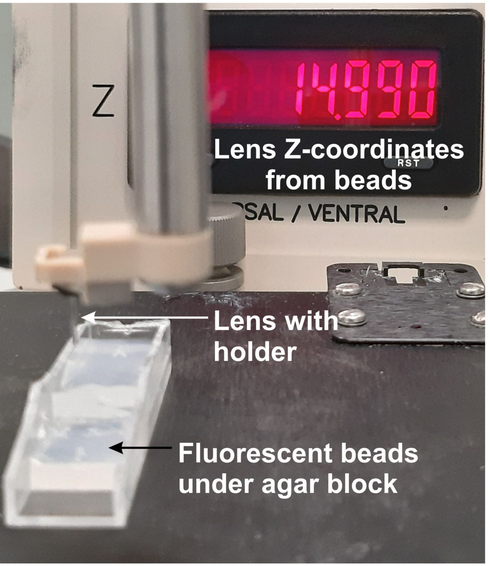

Camera Turret at 4 turns up

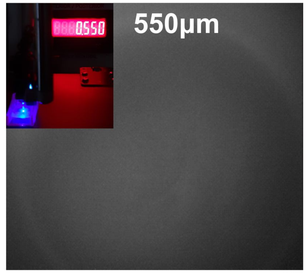

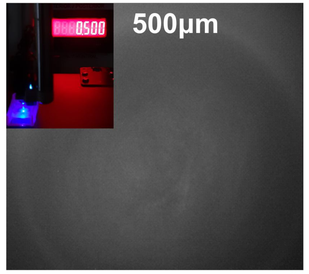

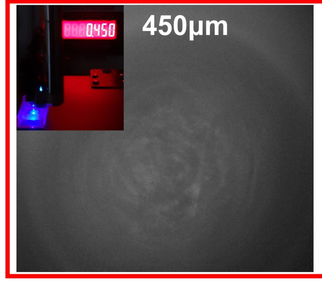

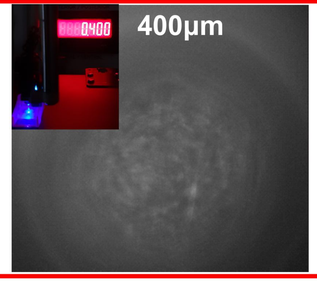

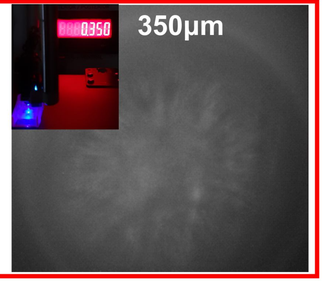

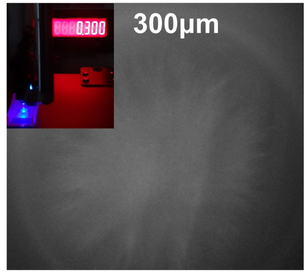

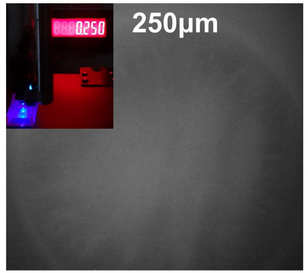

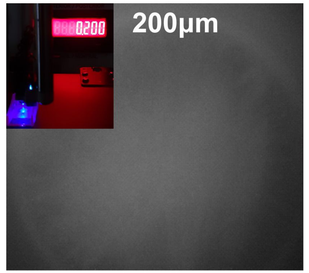

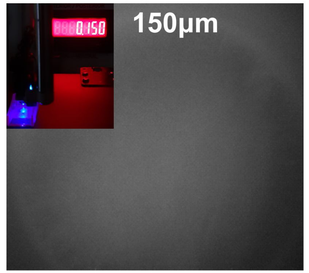

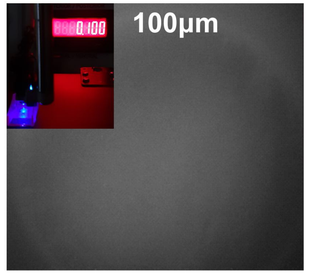

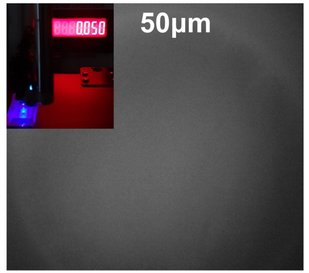

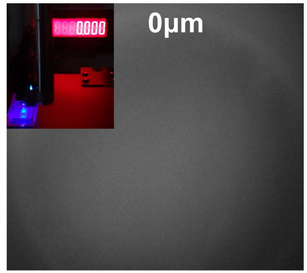

Camera Turret at 0 turns

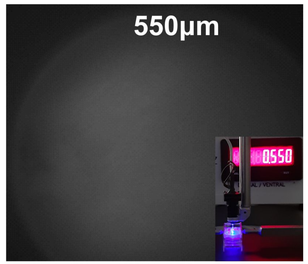

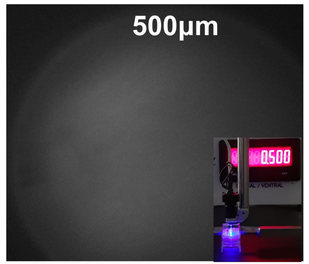

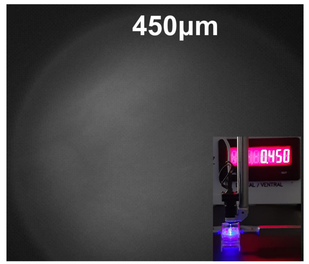

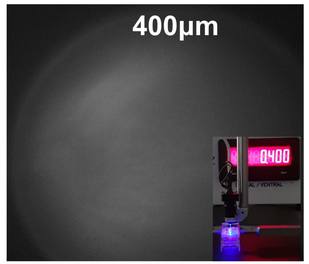

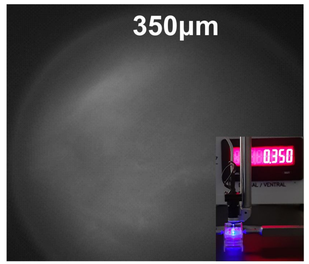

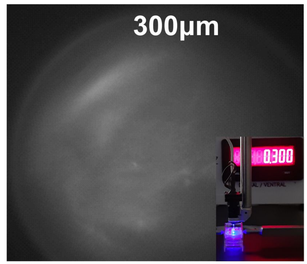

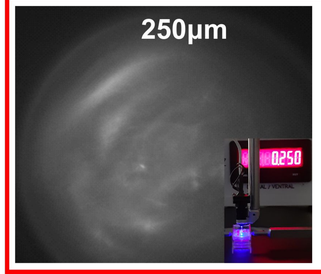

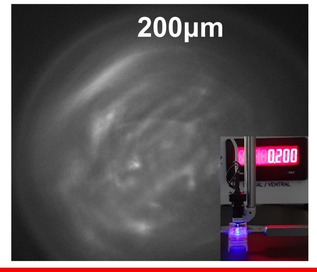

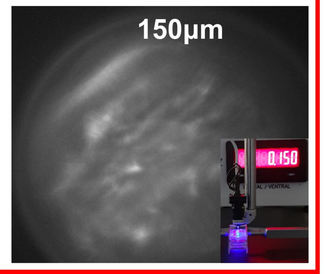

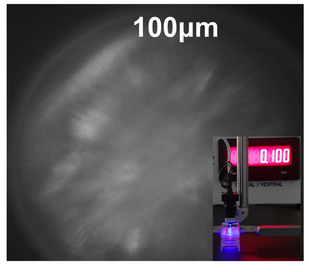

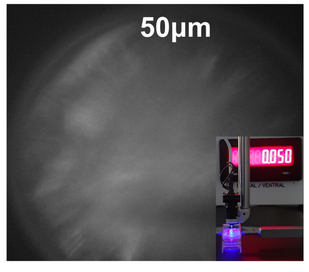

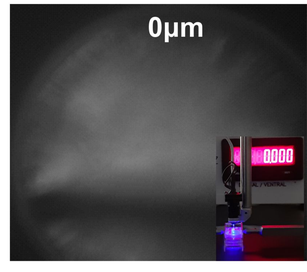

A. RTN Neuronal responses

Average E_G

GCaMP Fluor E_G

Average E_A

GCaMP Fluorescence E_A

Average I

GCaMP Fluorescence I

GCaMP Fluor Sn

GCaMP Fluor T

GCaMP Fluor NC-RR

GCaMP Fluorescence NC

T-4.0 T-3.0 T-3.0 T-0.0 T-2.0 T-1.25 T-2.0 T-3.0

T-3.75 T-2.0 T-3.75 T-1.25 T-3.0 T-3.0 T-3.0

T-0.0 T-2.0 T-3.0

1 min

1 min

1 min

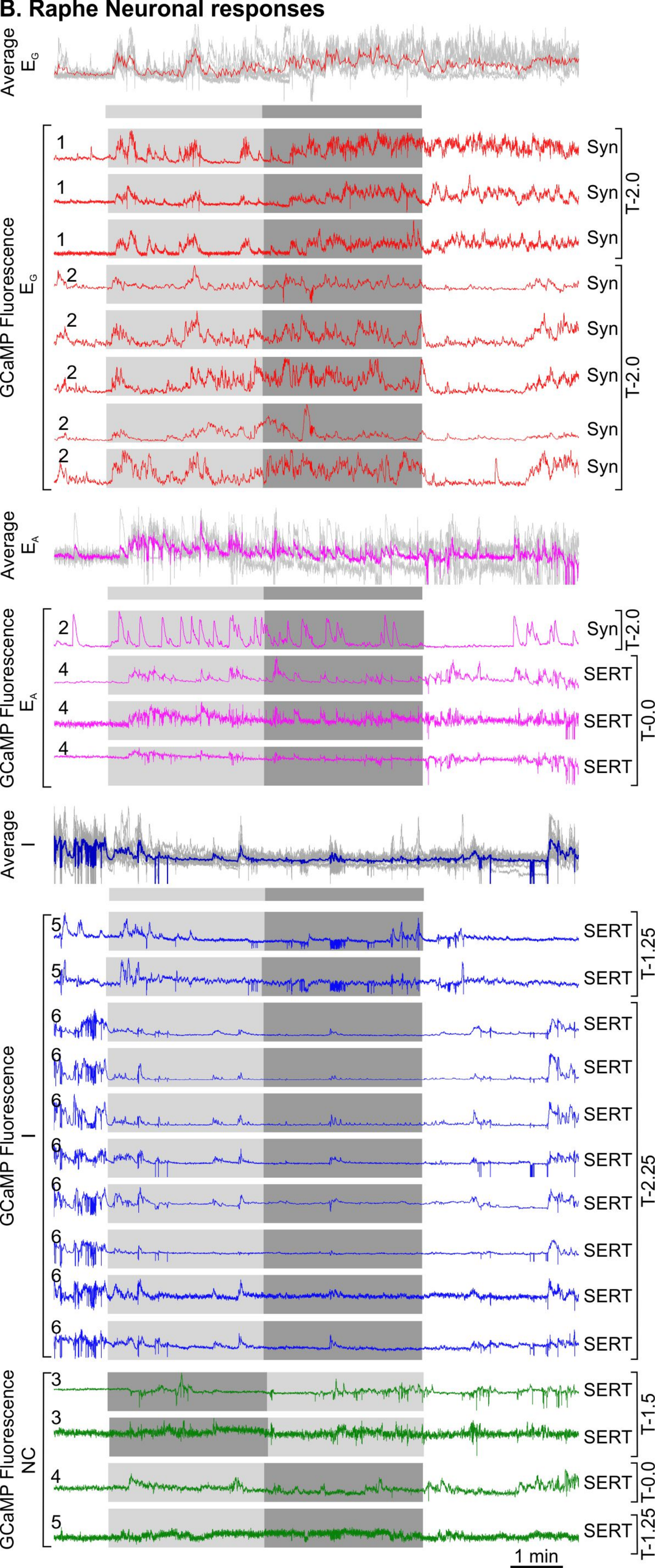
B. Raphe Neuronal responses
Average E_G
GCaMP Fluorescence E_G
1
2
Syn
T-2.0
Average E_A
GCaMP Fluorescence E_A
4
SERT
T-0.0
Average I
GCaMP Fluorescence I
5
6
T-1.25
T-2.25
GCaMP Fluorescence NC
3
4
5
T-1.5
1 min

C. pF_L Neuronal responses

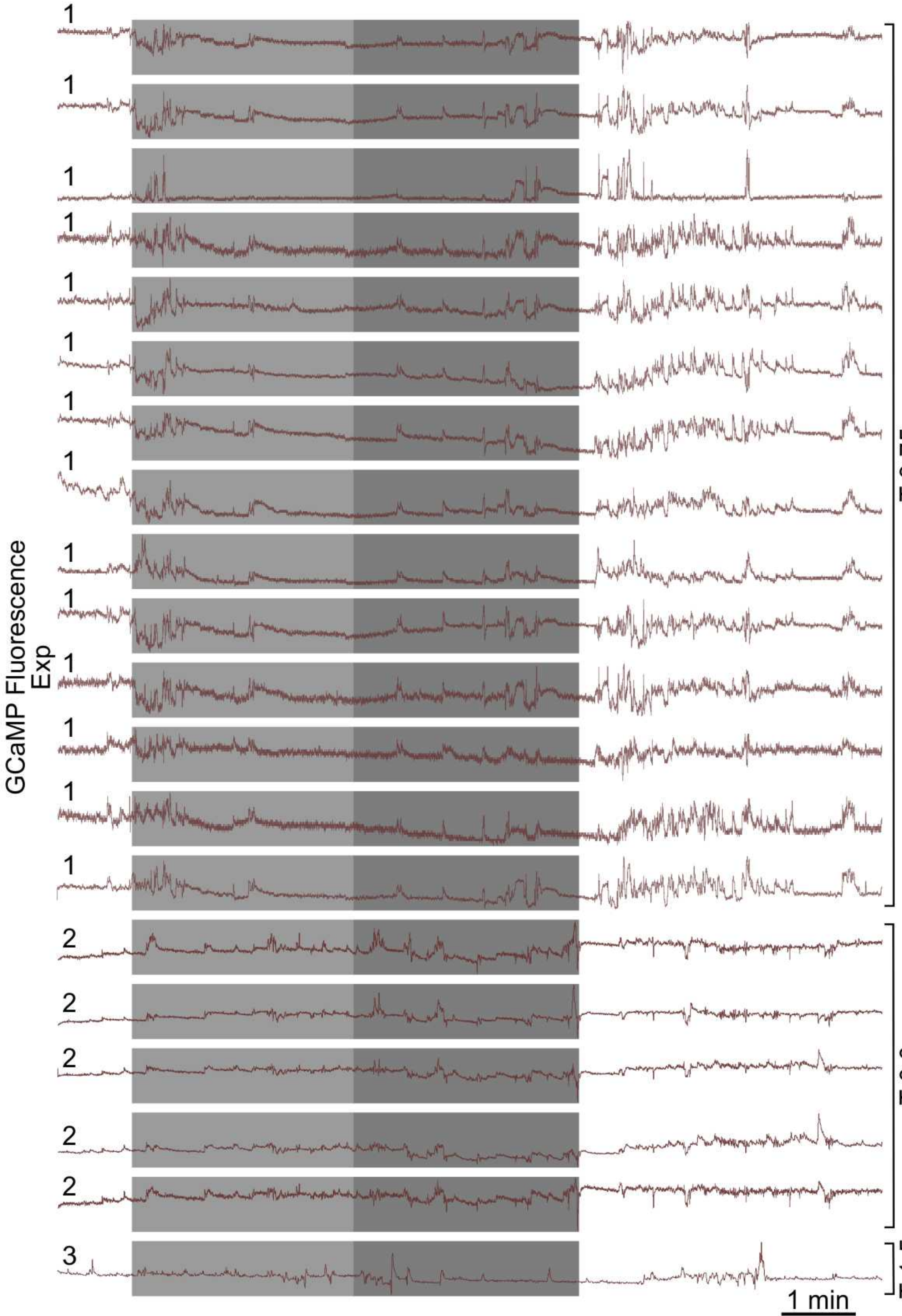

Session-A

Session-B

Mouse-2

I

Sn

Mouse-3

E_A

NC

Mouse-4

Fluorescence

GCaMP

Mouse-5

T

1 min

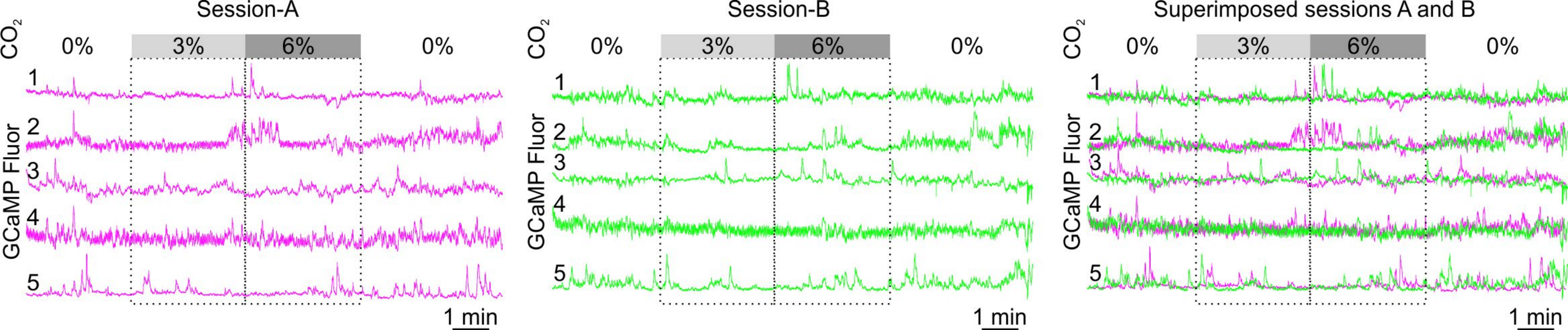
Session-A
Session-B
Superimposed sessions A and B
CO_2
0%
3%
6%
0%
GCaMP Fluor
1
2
3
4
5
1 min

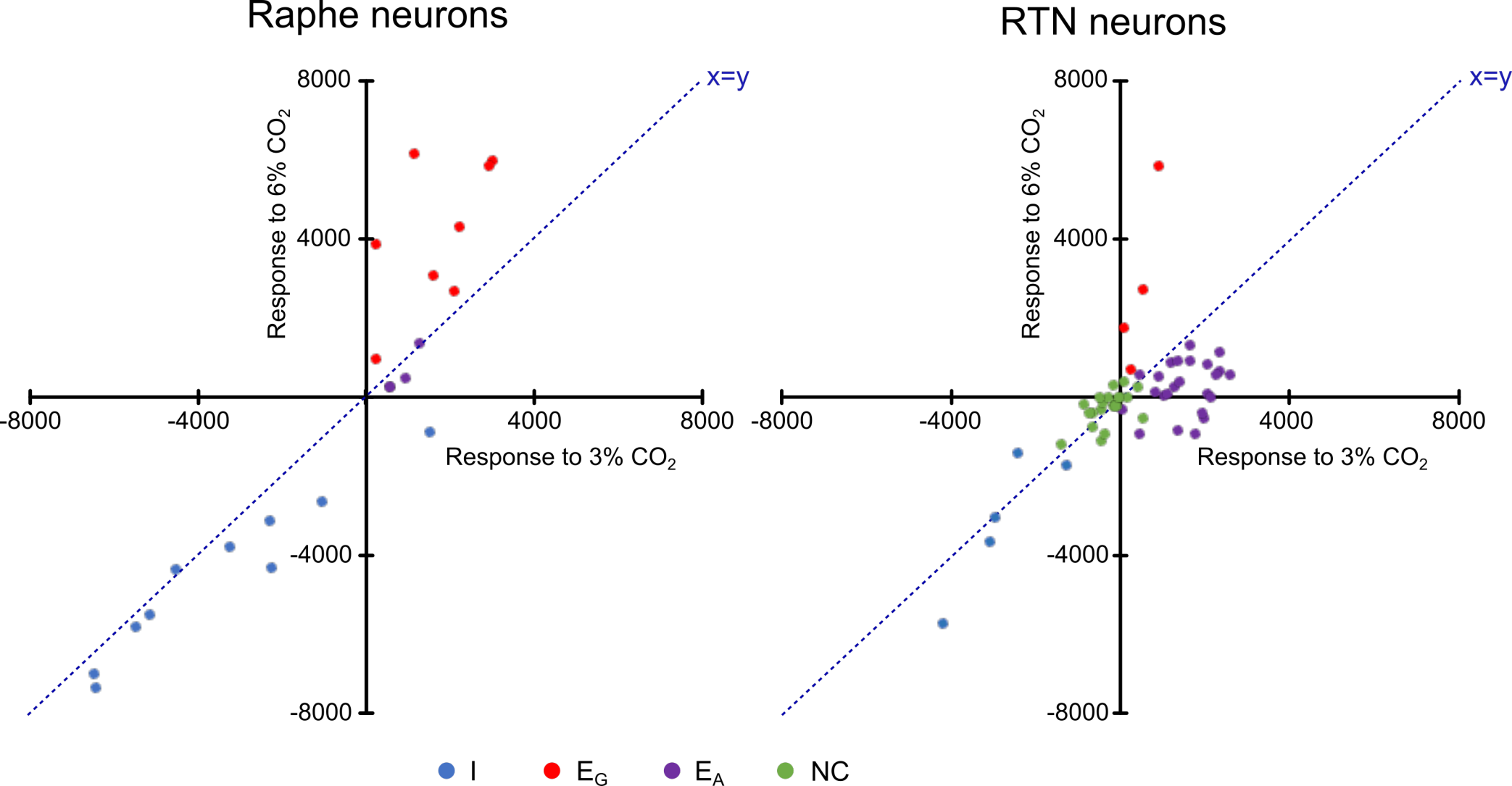
Raphe neurons
RTN neurons
x=y
Response to 6% CO2
Response to 3% CO2
8000
4000
-4000
-8000
I
EG
EA
NC

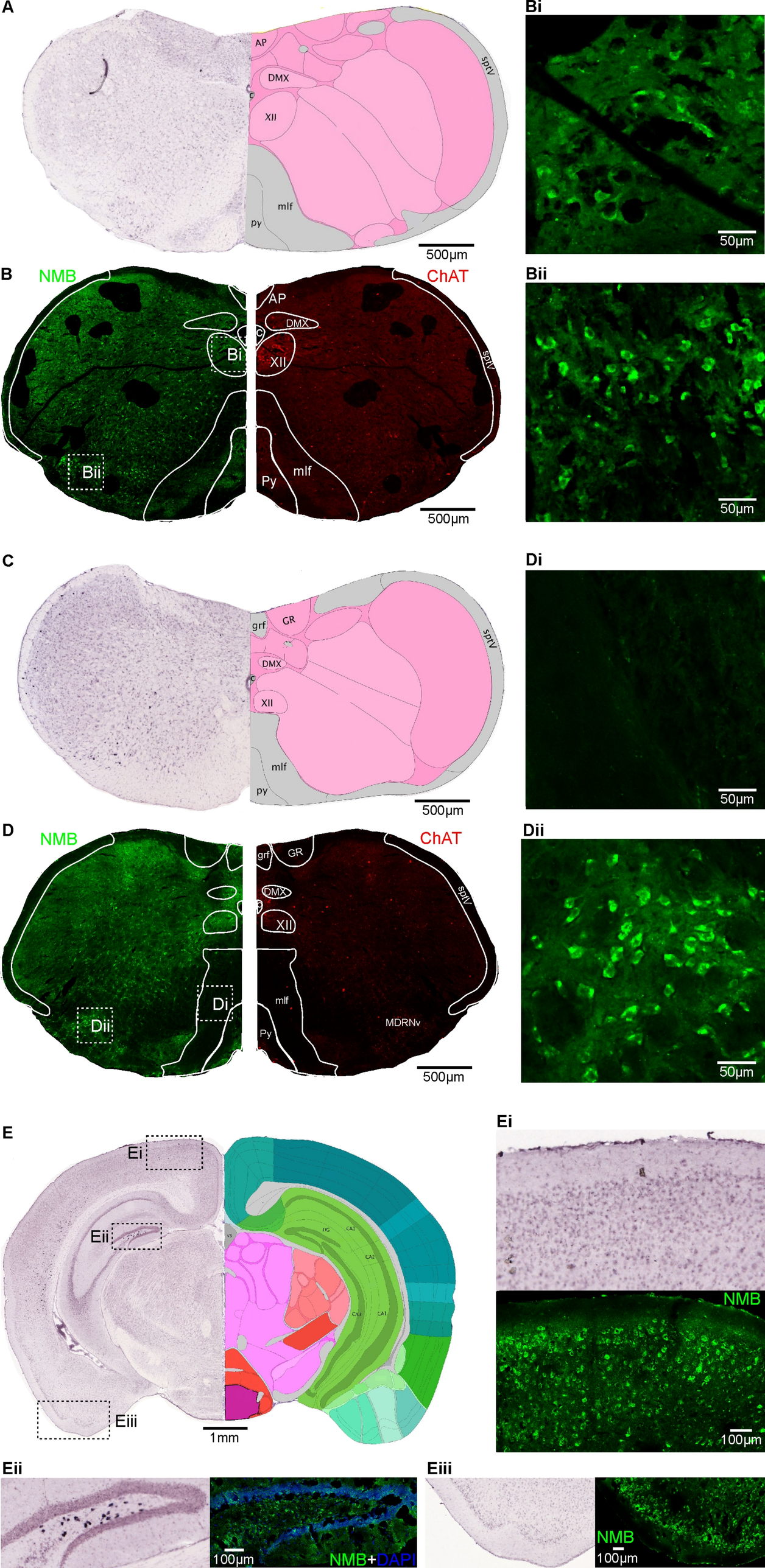
A
AP
DMX
XII
mlf
py
sptV
500µm
Bi
50µm
B
NMB
ChAT
AP
DMX
XII
Bi
Bii
Py
mlf
sptV
500µm
Bii
50µm
C
grf
GR
DMX
XII
mlf
py
sptV
500µm
Di
50µm
D
NMB
ChAT
grf
GR
DMX
XII
Di
Dii
mlf
Py
MDRNv
sptV
500µm
Dii
50µm
E
Ei
Eii
Eiii
1mm
Ei
NMB
100µm
Eii
100µm
NMB+DAPI
Eiii
NMB
100µm

0% CO_2
3% CO_2
6% CO_2
0% CO_2
1.03
E_A (F/F0)
1.00
0
min
13
1.03
E_A (F/F0)
1.00
0
Sec
8
Pre
3%
6%
Post

0% CO_2
3% CO_2
6% CO_2
0% CO_2
1.08
E_A (F/F0)
1.00
0
min
13
1.08
E_A (F/F0)
1.00
0
Sec
8
Pre
3%
6%
Post

0% CO_2
3% CO_2
6% CO_2
0% CO_2
1.03
E_A (F/F0)
1.00
0
min
13
1.03
E_A (F/F0)
1.00
0
Sec
8
Pre
3%
6%
Post

0% CO_2
3% CO_2
6% CO_2
0% CO_2
1.08
E_A (F/F0)
1.00
0
min
13
1.08
E_A (F/F0)
1.00
0
Sec
8
Pre
3%
6%
Post

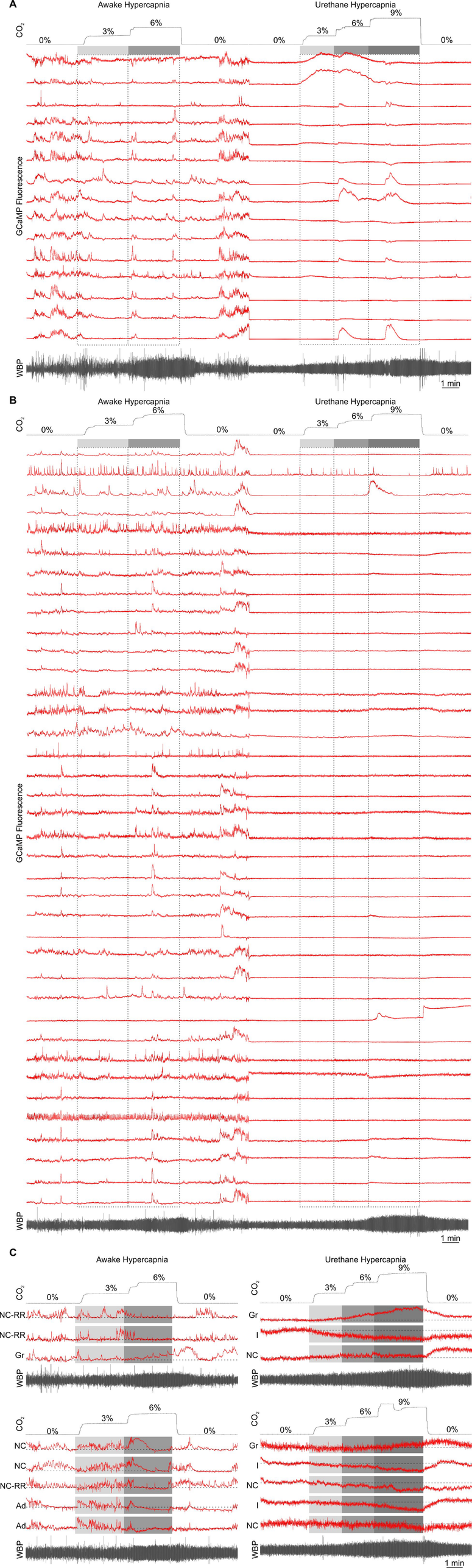
A
Awake Hypercapnia
Urethane Hypercapnia
CO2
0%
3%
6%
9%
GCaMP Fluorescence
WBP
1 min
B
Awake Hypercapnia
Urethane Hypercapnia
CO2
GCaMP Fluorescence
WBP
1 min
C
Awake Hypercapnia
Urethane Hypercapnia
CO2
NC-RR
Gr
WBP
NC
Ad
I
1 min

A. RTN Neurons

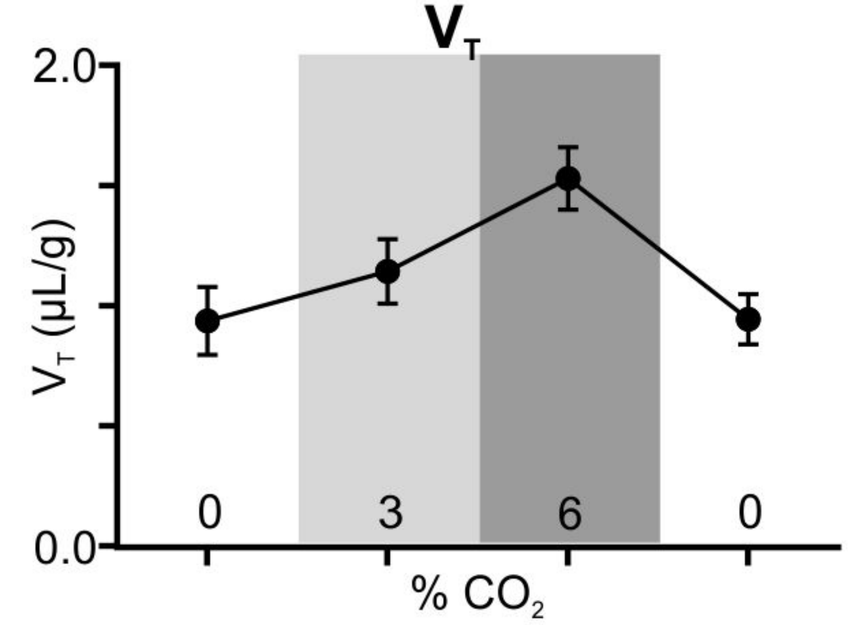

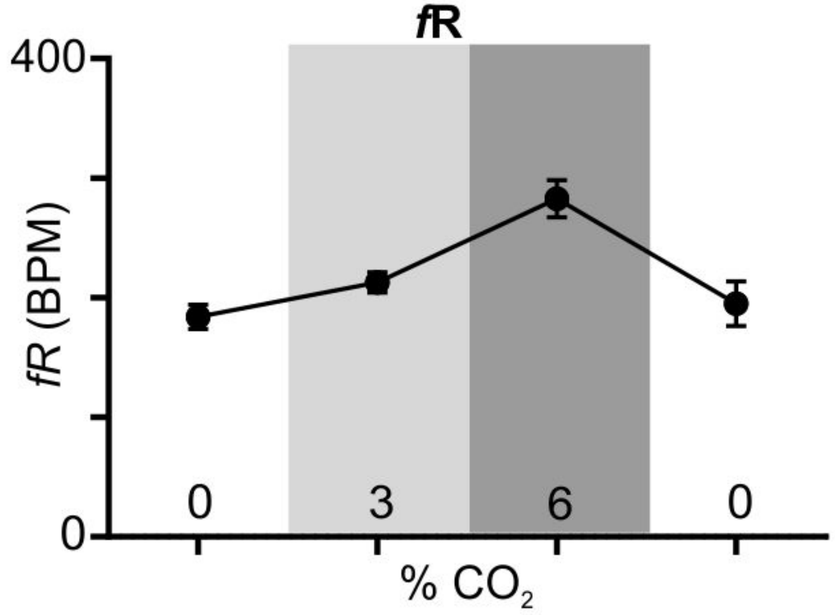

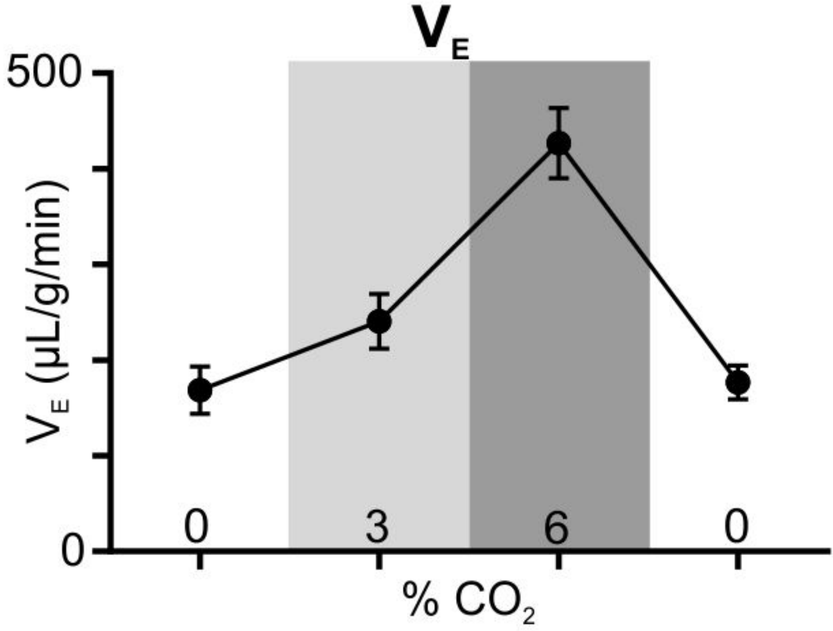

B. Raphe Neurons

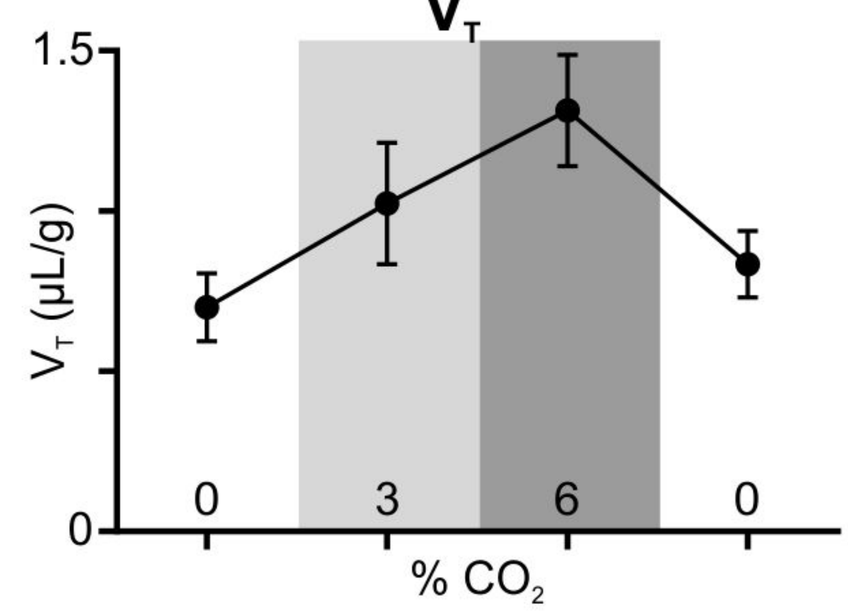

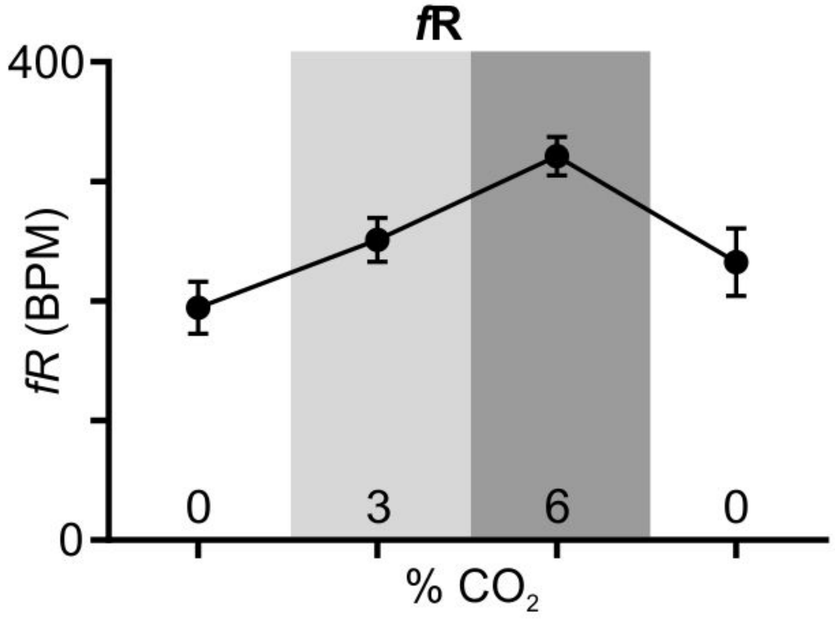

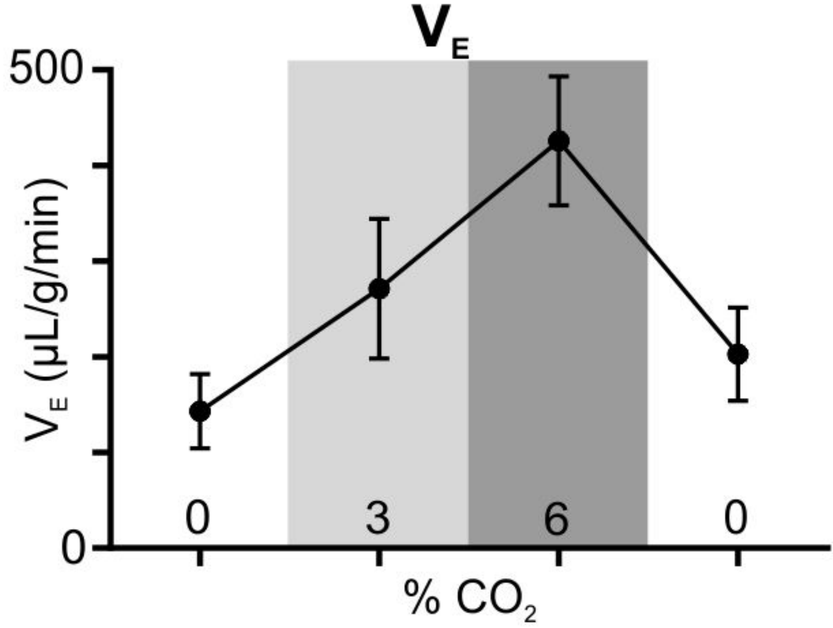

C. pF_L Neurons